Chapter 2

Femtosecond Laser Cavity Characterization

E. Nava-Palomares, F. Acosta-Barbosa, S. Camacho-López
and M. Fernández-Guasti

Additional information is available at the end of the chapter

http://dx.doi.org/10.5772/50174

1. Introduction

Ultrafast pulses are used now days in physics, engineering, medicine and other research areas such as, materials processing, time resolved spectroscopy, optical coherence tomography, pulse propagation, evolution of fast chemical processes, time resolved interference, etc. It is important to understand the physical processes that govern ultra fast laser pulse generation and shaping. In the present work, we characterize and find optimum operating conditions for a commercial Ti:Sa mode locked laser oscillator that generates pulses around 60 fs duration at 80 MHz repetition rate. Typical output power is 200 mW in mode locked operation.

The sharply peaked time structure at the oscillator output is explained in terms of the superposition of monochromatic waves with integer wavelength multiples of the round trip of the cavity. If a large number of waves with the same absolute phase are added with periodically shifted frequencies, the amplitude envelope becomes a periodically peaked train of temporal pulses. In Ti:Sa oscillators self mode-locking is achieved via Kerr lens mode-locking (KLM). The cavity is tuned so that self focusing of the more intense beam profile is favored.

The ultrafast oscillator is pumped by a Nd:YVO_4 CW laser. This laser is intra-cavity frequency doubled, the power output at 532 nm is 2.07 W. The pump beam is steered via two 45° mirrors into the IR cavity. The beam is focused into the Ti:Sa crystal with a 50 mm focal length lens as shown in figure 1. This beam passes through an IR convex mirror (C1) before reaching the active medium. The Ti:Sa emission resonates in a folded cavity comprising 2 concave mirrors and 6 plane mirrors. The group velocity dispersion (GVD) is compensated with a two prisms setup. A variable slit is placed between the back resonator mirror and the second prism. Figure 1 shows the Quantronix Ti-light laser layout and table 1 lists its main components. The oscillator together with an amplifier and a parametric generator were placed on a very stable passively damped holographic table [1].

In section 2, we revise the mathematical description of ultra short pulses. In particular, Gaussian pulses and hyperbolic secant pulses bringing together results that are scattered here

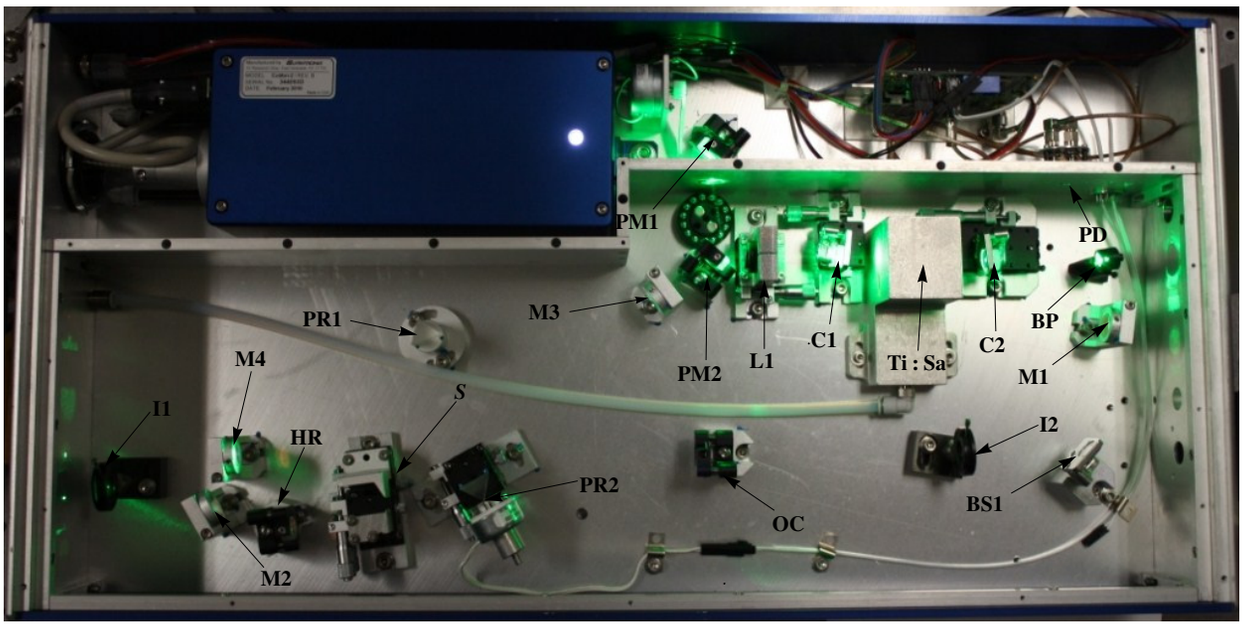

Figure 1. Ti:Sa laser at the Quantum Optics Laboratory, UAM-Iztapalapa

Components	Description
L1	pump beam focusing lens
C1, C2	first and second curved mirrors focused at crystal
M1- M4	IR Cavity folding mirrors
HR	rear highly reflective mirror
OC	output partially reflective mirror
Ti:Sa	Titanium Sapphire crystal
BS1	beam splitter
S	slit
PR1, PR2	first and second GVD compensating prisms
PM1, PM2	mirrors for 532 nm pump, reflection at 45°
I1, I2	iris
BD	beam dump
PD	photo diode

Table 1. Ti:Sa oscillator components.

and there in the literature. In subsection 2.4, the principles of mode-locked laser operation are glossed. Mode-locking is explained in terms of the superposition of monochromatic waves with integer wavelength multiples of the round trip of the cavity. The relevance of a broadband active medium is highlighted. The self mode-locking mechanism is described using the third order Kerr nonlinearity that leads to self focusing of the transverse Gaussian beam profile. The energy content of the output wave is described via a novel approach in subsection 2.5. This formulation avoids the averaging process required by either the Poynting vector or the irradiance functions proposed by Walther, Marchand, Wolf (WMW) and others.

In section 3, power output was measured as a function of mirror C2 position without mode locking. The laser output spectrum was also recorded for different mirror C2 positions within the mode locked regime (ML) with and without CW breakthrough.

In section 4, the pulse repetition rate was carefully measured in order to evaluate the cavity length. The internal photo diode as well as an external fast avalache photo diode were used to measure the pulse train. The difference between the mode locking peak intensity and the continuous CW background light was estimated. These measurements were also performed with much higher resolution using a streak camera.

In section 5, the pulse spectrum was monitored as a function of spectrum intra-cavity cropping. This was achieved through variation of the slit width (S-W) and slit translation (S-T). In section 5.1 the spectrum was evaluated as a function of GVD compensation. For this purpose, the second prism (PR2) position was varied and the spectrum was recorded.

In section 6, a second harmonic generation (SHG) frequency-resolved optical gating (FROG) setup was used to record the temporal features of the pulse: i) the pulse duration, ii) bandwidth, iii) pulse front tilt and iv) spatial chirp. Slit translation, width (S-T) and second prism (PR2) position were adjusted to achieve minimum time bandwidth product (TBP). The pulse measurements were fitted with appropriate curves and correlated to each other. The data obtained from these measurements together with their corresponding spectra from section 5 were fitted to Gaussian and hyperbolic secant time envelopes.

In the last section conclusions are drawn and the main results are abridged.

2. Theory of operation

2.1. Wave description

Ultrafast pulses are usually modeled by a carrier frequency modulated by a temporal envelope. This approach is usually adequate for pulses where the envelope duration is larger than a few oscillation periods. However, for pulses containing only a couple of periods, spatio temporal effects do not permit these type of solutions except for plane waves [2, 3]. It is customary to group the fast oscillating dependence in the phase function whereas the slowly varying features are grouped in a complex amplitude. This approach allows for slowly varying envelope approximations (SVEA) to be readily made [4]. However, a strict amplitude and phase representation requires that both of these functions are real. It is only under these circumstances that appropriate amplitude and phase functions can be used to establish an exact invariant [5].

The representation of a wave using complex variable in its polar representation is

$$\mathbf{E}\left(A,\Phi\right)=\mathbf{A}\exp\left(i\Phi\right), \tag{2.1}$$

where A is the amplitude and Φ is the phase, both of which are real valued functions. To represent a plane wave, the phase is a linear function of time and space, $\Phi=\omega t-\mathbf{k}\cdot\mathbf{r}$, where ω is the angular frequency, t represents time, $\mathbf{k}$ is the wave vector and $\mathbf{r}$ represents position. A plane wave with finite duration, is then described by a linear phase modulated by a time dependent amplitude $A\left(t\right)$

$$E\left(\mathbf{r},t\right)=A\left(t\right)\exp\left[i\left(\omega t-\mathbf{k}\cdot\mathbf{r}\right)\right]. \tag{2.2}$$

For the sake of simplicity, we shall focus on the temporal domain and neglect polarization effects. Pulsed Nd:YAG lasers usually have a Gaussian envelope. This profile is one of the few functions that can be tackled analitically in the time and frequency domains. On the other hand, ultrafast Ti:Sa lasers usually exhibit a profile closer to a hyperbolic secant curve. However, a hyperbolic secant with linear chirp cannot be solved analitically. For this reason, the problem has been tackled with a hyperbolic tangent chirp that is approximately linear in its central region. Analytical results in terms of Gamma functions can then be obtained. These two procedures are described in subsections 2.2 and 2.3.

2.2. Gaussian envelope

A Gaussian envelope has the form $A(t) = \exp\left(-\Gamma t^2\right)$, where $\Gamma = 1/\tau_G^2$. So the field (2.2) temporal function takes the form

$$E(t) = A_0 \exp\left(-\frac{t^2}{\tau_G^2}\right) \exp\left(i\omega_\ell t\right), \tag{2.3}$$

where ω_ℓ is a constant frequency. Figure 2 shows a plot of a Gaussian pulse. The intensity is defined as $I = |E|^2 = EE^*$, so the intensity of a Gaussian pulse without chirp in the temporal domain is given by the function (2.3) times its complex conjugate

$$I(t) = \frac{1}{2}\varepsilon_0 c\, nE(t)\, E^*(t) = A_0^2 \exp\left[-\frac{2t^2}{\tau_G^2}\right]. \tag{2.4}$$

Figure 4 shows the intensity in the temporal domain. The full width at half-maximum (FWHM) is obtained by equating at the time when the intensity falls to one half $I = 1/2$,

$$\exp\left[-2\left(\frac{t}{\tau_G}\right)^2\right] = \frac{1}{2},$$

The time half width at half maximum is then

$$\triangle t_{HWHM} = \sqrt{\frac{1}{2}\log(2)}\tau_G.$$

In order to get the full width at the half-maximum multiplication by two is required

$$\triangle t_{FWHM} = \sqrt{2\log(2)}\tau_G = 1.17741\tau_G. \tag{2.5}$$

To analyze the electric field in the spectral domain, the Fourier transform[1] is evaluated,

$$E(\Omega) = \frac{1}{\sqrt{2\pi}} \int_{-\infty}^{\infty} A_0 \exp\left(-\frac{t^2}{\tau_G^2} + i\omega_\ell t - i\Omega t\right) dt = \frac{A_0\tau_G}{\sqrt{2}} \exp\left(-\frac{\tau_G^2\left(\Omega - \omega_\ell\right)^2}{4}\right). \tag{2.6}$$

[1] $E(\Omega) = \frac{1}{\sqrt{2\pi}} \int_{-\infty}^{\infty} \mathcal{E}(t) \exp\left[-i\Omega t\right] dt$

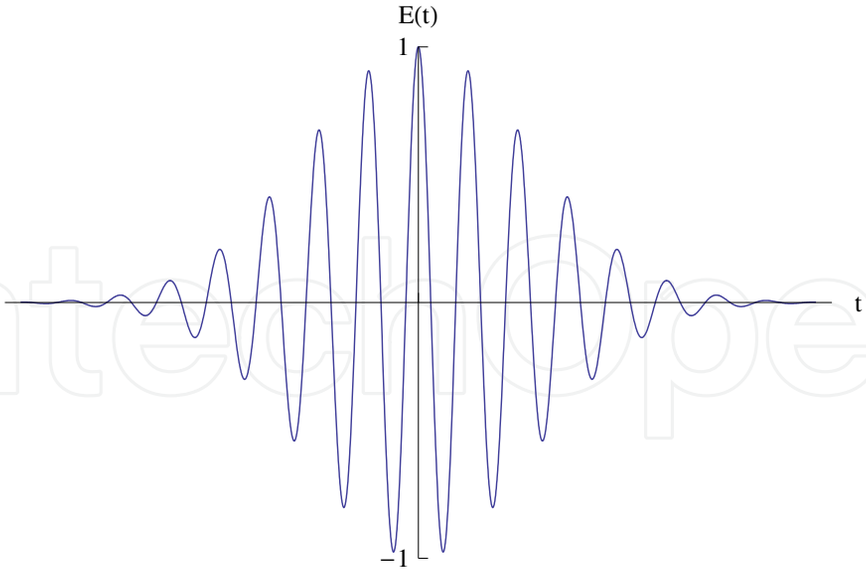

Figure 2. Gaussian pulse.

The intensity in the frequency domain for a Gaussian pulse without chirp is

$$I(\Omega) = \frac{1}{2}\varepsilon_0 c\, n \frac{A_0^2 \tau_G^2}{2} \exp\left[-\frac{\tau_G^2 (\Omega - \omega_\ell)^2}{2}\right]. \tag{2.7}$$

The normalized intensity is obtained upon division by $|E(0)|^2$. The FWHM in the frequency domain is obtained in an analogous fashion as before. The bandwidth measured from the carrier frequency $\triangle\omega_{HWHM} = \triangle\Omega_{HWHM} - \omega_l = \triangle\Omega_{HWHM}$

$$\exp\left[\frac{-\tau_G^2 (\triangle\omega_{HWHM})^2}{2}\right] = \frac{1}{2}.$$

The full width at half maximum is twice the solution to this equation

$$\triangle\omega_{FWHM} = \frac{2\sqrt{2\log(2)}}{\tau_G} = \frac{2.3548}{\tau_G}. \tag{2.8}$$

2.2.1. Gaussian with chirp

Let us now consider a Gaussian pulse with a quadratic phase

$$\Phi(t) = \omega_\ell t - \frac{a}{\tau_G^2} t^2. \tag{2.9}$$

Its instantaneous frequency is given by

$$\omega(t) = \frac{\partial\Phi}{\partial t} = \omega_\ell - \frac{1}{2}\frac{a}{\tau_G^2} t. \tag{2.10}$$

This means that the frequency is time dependent and the pulse is say to be chirped, a is the chirp factor. Figure 3 shows the plot of a chirped Gaussian pulse. With the present sign

conventions i.e. eq. (2.10), the chirp factor is positive for down-chirp (frequency decreasing in time) and negative for up-chirp (frequency increasing in time). The electric field for a chirped pulse in the time domain is

$$E(t) = A_0 \exp\left[-(1+ia)\frac{t^2}{\tau_G^2} + i\omega_\ell t\right]. \tag{2.11}$$

The intensity in the time domain of the Gaussian chirped pulse is identical to the Gaussian pulse without chirp (2.4). That is, the time dependent intensity does not depend of the chirp constant.

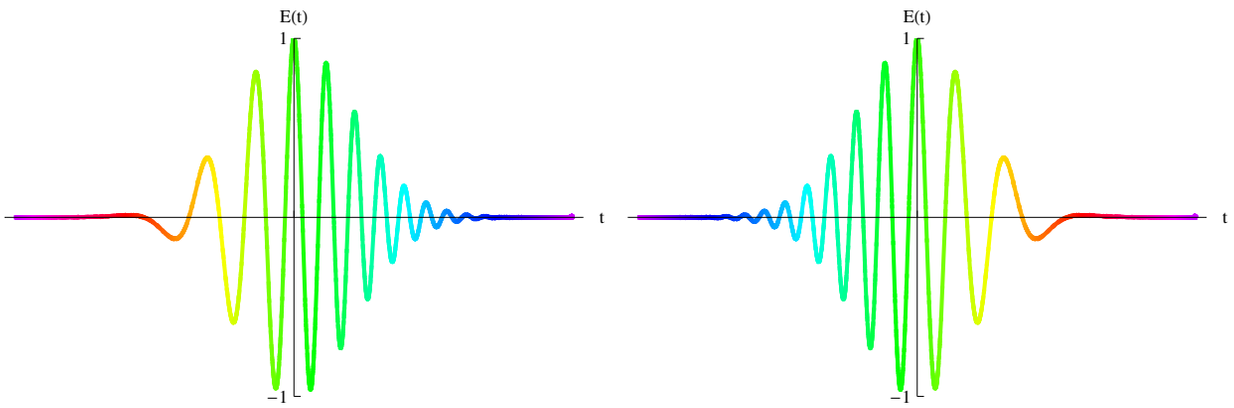

(a) Up-chirp: Negative chirp parameter $a = -3$

(b) Down-chirp: Positive chirp parameter $a = 3$

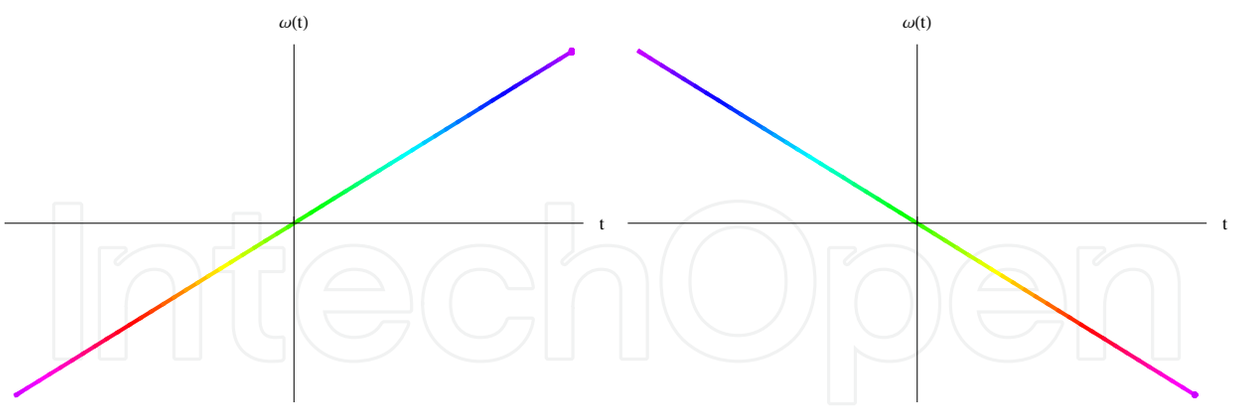

(c) For up-chirp, $a < 0$, the instantaneous frequency has positive slope.

(d) For down-chirp, $a > 0$, the instantaneous frequency has negative slope.

Figure 3. Chirped Gaussian pulse.

The Fourier transform of the quadratic time dependence (2.11) is

$$\tilde{E}(\Omega) = \frac{1}{\sqrt{2\pi}} \int_{-\infty}^{\infty} A_0 \exp\left[-(1+ia)\frac{t^2}{\tau_G^2}\right] \exp(-i\Omega t)\, dt,$$

upon integration

$$\tilde{E}(\Omega) = \frac{A_0}{\sqrt{2}} \frac{\tau_G}{\sqrt{(ia+1)}} \exp\left(\frac{i\Omega\tau_G^2}{4(a-i)}\right). \tag{2.12}$$

This equation can be written as

$$\tilde{E}(\Omega) = E(\Omega) = \frac{A_0}{\sqrt{2}} \frac{\tau_G}{\sqrt[4]{(1+a^2)}} \exp\left[i\phi - \frac{\omega^2\tau_G^2}{4(a^2+1)}\right], \tag{2.13}$$

where $\phi = \left(\frac{1}{2}\arctan(a) + \frac{a\Omega^2\tau_G^2}{4(a^2+1)}\right)$. On the other hand, the intensity in the frequency domain is $I(\Omega) = \varepsilon_0 c\, n\tilde{E}(\Omega)\,\tilde{E}^*(\Omega)$

$$I(\Omega) = \frac{1}{2}\varepsilon_0 c\, n\varepsilon_0 c\, n\frac{A_0^2}{2} \frac{\tau_G^2}{\sqrt[2]{(1+a^2)}} \exp\left[i\phi - \frac{\Omega^2\tau_G^2}{4(1+a^2)}\right] \exp\left[-i\phi - \frac{\Omega^2\tau_G^2}{4(1+a^2)}\right],$$

$$I(\Omega) = \varepsilon_0 c\, n\frac{A_0^2}{4} \frac{\tau_G^2}{\sqrt[2]{(1+a^2)}} \exp\left[-\frac{\Omega^2\tau_G^2}{2(1+a^2)}\right], \tag{2.14}$$

and the normalized frequency dependent intensity is

$$I(\Omega) = \exp\left[-\frac{\Omega^2\tau_G^2}{2(1+a^2)}\right]. \tag{2.15}$$

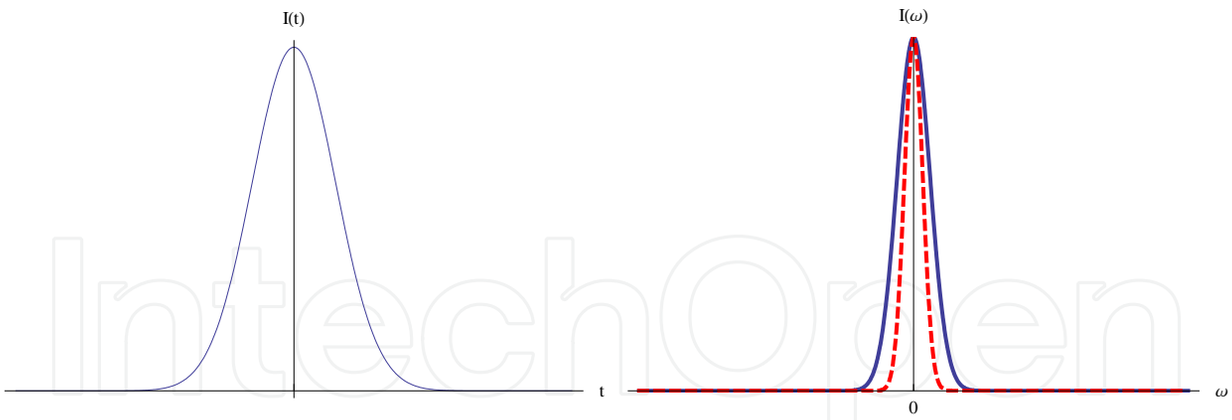

(a) Intensity of a Gaussian pulse with and without chirp in the temporal domain (curves are overlapped).

(b) Intensity of a Gaussian pulse with (solid) and without chirp (dashed) in the frequency domain.

Figure 4. Gaussian chirped pulse.

2.2.2. Time bandwidth product

The time bandwidth product of a Gaussian pulse without chirp from (2.5) and (2.8) is

$$(\triangle t \triangle\omega)_{FWHM} = \sqrt{2\log(2)}\tau_G \frac{2\sqrt{2\log(2)}}{\tau_G} \approx 2.2226, \tag{2.16}$$

or in terms of the frequency

$$(\triangle t \triangle \nu)_{FWHM} = \frac{2\log(2)}{\pi} \approx 0.4413\,. \tag{2.17}$$

For a Gaussian chirped pulse, the FWHM in the temporal domain is the same as the Gaussian pulse without chirp. However, the FWHM in the frequency domain for the chirped pulse is obtained from (2.15)

$$\exp\left[-\frac{\triangle\omega_{HWHM}^2\tau_G^2}{2\left(1+a^2\right)}\right] = \frac{1}{2}.$$

The frequency FWHM in the frequency domain for a Gaussian chirped pulse is then

$$\triangle\omega_{FWHM} = \frac{\sqrt{8\left(1+a^2\right)\log(2)}}{\tau_G}. \tag{2.18}$$

The time bandwidth product from (2.5) and (2.18) is

$$(\triangle t \triangle \omega)_{FWHM} = 4\log(2)\sqrt{1+a^2}, \tag{2.19}$$

or in terms of the linear frequency

$$(\triangle t \triangle \nu)_{FWHM} = \frac{2\log(2)}{\pi}\sqrt{1+a^2}. \tag{2.20}$$

To abridge, a Gaussian pulse with linear frequency chirp produces a Gaussian spectral distribution broadened by $\sqrt{1+a^2}$. The time bandwidth product increases by this same amount since the temporal width is unaltered.

2.3. Hyperbolic secant envelope

2.3.1. Phase function without chirp

The electric field with carrier frequency $\frac{d\Phi(t)}{dt} = \omega_\ell$ modulated by a hyperbolic secant envelope $A(t)$ is

$$E(t) = A(t)e^{i\omega_\ell t} = \operatorname{sech}\left(\frac{t}{\tau_s}\right)e^{i\omega_\ell t}.$$

The time dependent intensity is

$$I(t) = \varepsilon_0 c\, n\, |A(t)|^2 = \varepsilon_0 c\, n \operatorname{sech}^2\left(\frac{t}{\tau_s}\right).$$

The time $\triangle t_{HWHM}$ where the intensity is at half maximum is

$$\operatorname{sech}^2\left(\frac{\triangle t_{HWHM}}{\tau_s}\right) = \frac{1}{2} \quad \Rightarrow \quad \triangle t_{HWHM} = \operatorname{arcsech}\sqrt{\frac{1}{2}}\tau_s = 0.881374\tau_s.$$

The intensity full width at half maximum is twice this value

$$\triangle t_{FWHM} = 2\text{arcsech}\sqrt{\frac{1}{2}}\tau_s \approx 1.76275\tau_s.$$

The field spectrum is obtained from the Fourier transform of the field

$$E(\Omega) = \mathcal{F}\{E(t)\} = \sqrt{\frac{\pi}{2}}\tau_s \text{sech}\left(\frac{\pi\tau_s(\omega_\ell + \Omega)}{2}\right),$$

the frequency dependent intensity is then

$$I(\Omega) = |E(\Omega)|^2 = \varepsilon_0 c\, n \frac{\pi}{4}\tau_s^2 \text{sech}^2\left(\frac{\pi\tau_s(\omega_\ell + \Omega)}{2}\right). \tag{2.21}$$

The maximum intensity is reached when $\Omega = \omega_\ell$, then $I_M = \varepsilon_0 c\, n \frac{\pi}{4}\tau_s^2$. The frequency $\Delta\Omega_{HM} = \omega_\ell + \Omega_{HM}$ where the intensity is at half maximum is then

$$\frac{\pi}{2}\tau_s^2 \text{sech}^2\left(\frac{\pi\tau_s(\Delta\Omega_{HM})}{2}\right) = \frac{\pi}{4}\tau_s^2.$$

The frequency FWHM is then

$$\Delta\Omega_{FWHM} = \frac{4}{\pi\tau_s}\text{arcsech}\left(\sqrt{\frac{1}{2}}\right).$$

The Time-bandwidth product is thus

$$\Delta\Omega_{FWHM}\triangle t_{FWHM} = \left(\frac{4}{\pi\tau_s}\text{arcsech}\left(\sqrt{\frac{1}{2}}\right)\right)\left(2\text{arcsech}\sqrt{\frac{1}{2}}\tau_s\right) \approx 1.979.$$

In terms of the linear frequency

$$TBP = \Delta\nu_{FWHM}\triangle t_{FWHM} = \left(\frac{4}{2\pi^2\tau_s}\text{arcsech}\left(\sqrt{\frac{1}{2}}\right)\right)\left(2\text{arcsech}\sqrt{\frac{1}{2}}\tau_s\right) \approx 0.3148\,. \tag{2.22}$$

2.3.2. Phase function with chirp

For a pulse with linear chirp $\frac{d\Phi}{dt} = -\frac{2at}{\tau_s^2}$, the phase is quadratic in time $\Phi(t) = \omega_\ell - \frac{at^2}{\tau_s^2}$. The representation of the chirped pulse with hyperbolic secant envelope is then

$$E(t) = A(t)e^{i\Phi} = \text{sech}\left(\frac{t}{\tau_s}\right)\exp\left[i\left(\omega_\ell t + \frac{at^2}{\tau_s^2}\right)\right].$$

The Fourier transform $\mathcal{F}$ of the function with linear chirp cannot be solved analytically, so a different approach is presented. The frequency rate of change is a measure of the frequency deviation as a function of time $\frac{d\Phi(t)}{dt}$. The spectral width of solid state laser systems can be

described via laser rate equations [6]. The refractive index variation arising from the rate equation can describe frequency chirping [7]. This model can be used to describe a nonlinear chirp for hyperbolic secant pulses that is mathematically tractable. The phase equation in terms of laser intensity is [8]

$$\frac{d\Phi(t)}{dt} = \frac{a}{2}\frac{1}{I}\frac{dI}{dt},$$

where a is the phase amplitude coupling factor that will correspond to the chirp parameter as we shall presently see. For $I = \varepsilon_0 c\, n\, \text{sech}^2\left(\frac{t}{\tau_s}\right)$,

$$\frac{d\Phi(t)}{dt} = \frac{a}{2}\left(-\frac{2}{\tau_s}\tanh\left(\frac{t}{\tau_s}\right)\right) = -\frac{a}{\tau_s}\tanh\left(\frac{t}{\tau_s}\right).$$

The Gaussian profile with linear chirp and the hyperbolic secant profile with hyperbolic tangent chirp are similar near the central frequency for time $t \ll \tau_s$, $\frac{d\Phi(t)}{dt} = \left(-\frac{a}{\tau_s^2}t\right)$ as can be seen in figure 5.

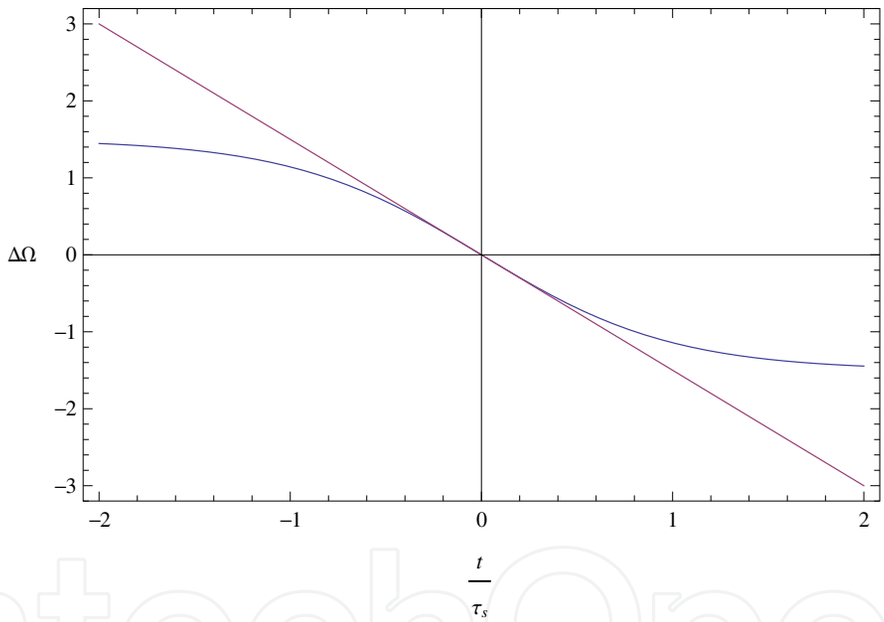

Figure 5. Instantaneous frequency deviation for a hyperbolic tangent chirp and a linear chirp.

The field phase can be obtained by direct integration

$$\frac{d\Phi(t)}{dt} = \frac{a}{2}\frac{1}{I}\frac{dI}{dt} = \frac{a}{2}\frac{d\ln I}{dt} = \frac{d}{dt}\ln I^{\frac{a}{2}}$$

so that $\Phi(t) = \ln I^{\frac{a}{2}}(t)$. Since $I(t) = |E(t)|^2 = \varepsilon_0 c\, n\, \text{sech}^2\left(\frac{t}{\tau_s}\right)$, the phase is then

$$\Phi(t) = \ln\left[\text{sech}^a\left(\frac{t}{\tau_s}\right)\right].$$

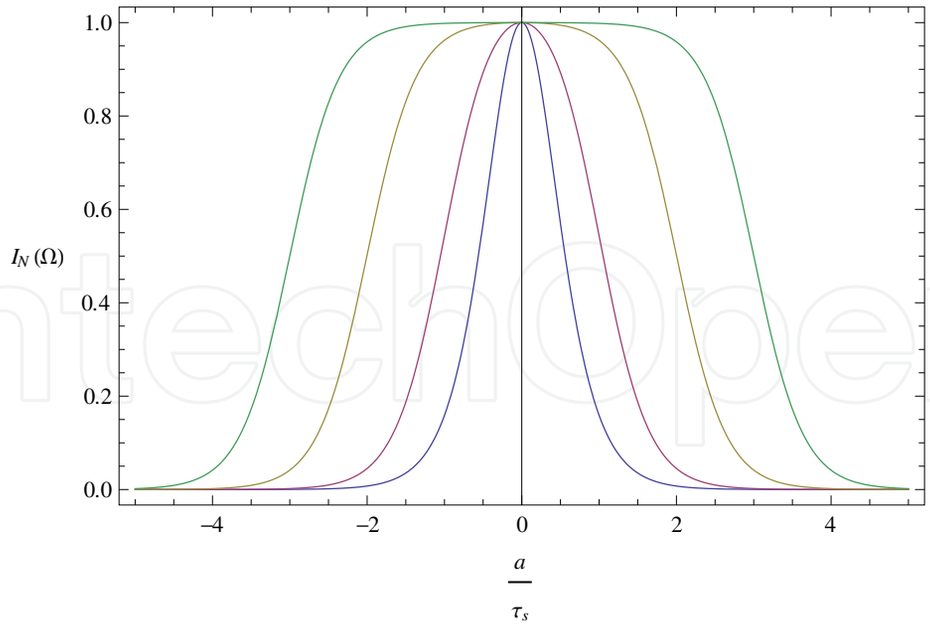

Figure 6. Different profiles as a function of chirp parameter a: 0, 1 ,2, 3 with increasing width and flattened top.

The complete electric field is therefore

$$E(t) = A(t)e^{i\Phi(t)} = \text{sech}\left(\frac{t}{\tau_s}\right)\exp\left[i\left\{\ln\left[\text{sech}^a\left(\frac{t}{\tau_s}\right)\right]\right\}\right],$$

that can be economically written as

$$E(t) = \text{sech}^{1+ia}\left(\frac{t}{\tau_s}\right). \tag{2.23}$$

The electric field for a non-linearly chirped pulse is thus described by a hyperbolic secant function raised to a complex power. The imaginary part corresponds to the chirp parameter. The Fourier transform of this function has an analytical solution in terms of Gamma functions with complex argument:

$$E(\Omega) = \mathcal{F}\{E(t)\} = \frac{2^{ia}\tau_s}{\Gamma(1+ia)}\Gamma\left(\frac{1+ia+i\Omega\tau_s}{2}\right)\Gamma\left(\frac{1+ia-i\Omega\tau_s}{2}\right).$$

The normalized power spectrum can then be written as

$$\frac{|E(\Omega)|^2}{|E(0)|^2} = \frac{\text{sech}\left[\frac{\pi}{2}(\Omega\tau_s + a)\right]\text{sech}\left[\frac{\pi}{2}(\Omega\tau_s - a)\right]}{\text{sech}^2\left(\frac{\pi a}{2}\right)}. \tag{2.24}$$

This function is plotted in figure 6 for various chirp parameters. The envelope flattens on the top as the chirp parameter is increased. Notice that when $a = 0$ (unchirped pulse) we obtain simply the previous $\text{sech}^2\left[\frac{\pi}{2}\Omega\tau_s\right]$ power spectrum.

2.4. Mode-locking mechanism

Phase locked laser operation requires a coherent superposition of waves with a well defined phase relationship. The waves have frequencies separated by the cavity round trip time inverse. Each mode has the form

$$E_j = Ae^{i(\omega_0 t + j\delta\omega t)},$$

where $\delta\omega$ is the frequency separation between modes and A is the amplitude of each mode. The modes amplitudes may be considered constant and equal in a first approximation within the gain bandwidth. However, they will obviously fall down at the edges of the medium's bandwidth.

2.4.1. Coherent sum of fields

The mode-locked cavity can be explained in terms of the superposition of monochromatic waves with integer wavelength multiples of the round trip of the cavity. The sum of m_{tot} waves traveling in the same direction (labeled with subindex $\Rightarrow$) with constant amplitude A in complex notation is

$$G_{\Rightarrow}e^{i\gamma_{\Rightarrow}} = \sum_{j=m_i}^{m_f} Ae^{i(\omega t + j\delta\omega t)}, \tag{2.25}$$

where $\delta\omega = 2\pi\delta v$, m_i is the initial mode and m_f is the final mode. Waves do not interact directly between them. However, they are actually added in the presence of charges that respond to the superposition of the fields [9]. In this case, it is within the Ti:Sa crystal where the summation is carried out

$$G_{\Rightarrow}e^{i\gamma_{\Rightarrow}} = A\frac{\sin\left(\frac{\left(m_f - m_i + 1\right)\delta\omega t}{2}\right)}{\sin\left(\frac{\delta\omega t}{2}\right)}\exp\left[i\left(\omega t + \frac{\left(m_f + m_i\right)}{2}\delta\omega t\right)\right]. \tag{2.26}$$

The amplitude is now time dependent with a periodicity $\frac{\delta\omega t}{2} = 2\pi b$ where b is an integer. The amplitude maxima are obtained from L'hopital rule, the magnitude is

$$G_{\Rightarrow max} = A\left.\frac{\cos\left(\frac{m_{tot}\delta\omega t}{2}\right)}{\cos\left(\frac{\delta\omega t}{2}\right)}\frac{\frac{m_{tot}\delta\omega}{2}}{\frac{\delta\omega}{2}}\right|_{\frac{\delta\omega t}{2}=2\pi} = Am_{tot}, \tag{2.27}$$

where $m_{tot} = m_f - m_i + 1$ is the total number of modes. Therefore, if a large number of waves with the same absolute phase are added with periodically shifted frequencies, the amplitude envelope becomes a periodically peaked train of temporal pulses. For an estimate of the width, consider the first zero of the amplitude function in (2.26), that is $\frac{m_{tot}\delta\omega\triangle t_0}{2} = \pi$. The full width between the first positive and negative zero of the function is

$$\triangle t_{FW0} = \frac{1}{\delta\nu}\frac{2}{m_{tot}} \tag{2.28}$$

Series expansion of the amplitude function is

$$\frac{\sin\left(\frac{m_{tot}\delta\omega\, t}{2}\right)}{\sin\left(\frac{\delta\omega\, t}{2}\right)} = m_{tot} - \frac{\delta\omega^2}{24}\left(m_{tot}^3 - m_{tot}\right)t^2 + \cdots$$

FWHM estimated from this series for large m_{tot} is

$$\triangle t_{FWHM} = \frac{1}{2\pi\delta\nu}\frac{4\sqrt{3}}{m_{tot}} \tag{2.29}$$

Three mechanisms are invoked in laser cavities in order to amplify the mode locked peaks: active feedback - pumping, intra-cavity saturable absorber and self mode-locking via self focusing. In Ti:Sa oscillators self mode-locking is the mechanism responsible for pulse generation. It is achieved via Kerr lens mode-locking (KLM). Kerr refractive index modulation is a third order nonlinear process where the refractive index is proportional to the intensity of the incoming beam $n = n_0 + n_2 I$. The cavity is tuned so that self focusing of the more intense beam profile is favored. In our setup, the second curved mirror (C2) distance from the Ti:Sa crystal is varied in order to achieve the mode-locking regime. The continuous light (CW) pump is a frequency-doubled Nd:YVO_4 laser at 532 nm with 2.07 W.

2.5. Energy content

In electromagnetic phenomena, Poynting's theorem is considered to represent the field energy conservation equation. However, the conservation equation obtained either from Maxwell's equations or the wave equation is not unique. The choice of Poynting's conservation equation as representing the electromagnetic energy is to some extent arbitrary and not exempt of counterintuitive predictions [10, p.27-6]. The Wigner function wave description [11, p.287] involves the function times its conjugate; Therefore, it also relies on a complex version of Poynting's energy theorem.

Another conservation equation derived from the wave equation is obtained by invoking the two linearly independent solutions [12]. These two wave solutions are referred to as the complementary fields. The complementary fields approach to wave phenomena requires the existence of two fields that establish a dynamical balance between two forms of energy. The energy content of the wave goes from one field to the other and back such that the total energy is constant for an infinite wave-train [13]. The formalism attempts to address two issues: i) a representation that avoids taking time averages and hence is suitable to describe ultrafast phenomena and ii) a description that gives a clearer picture of the apparent redistribution of energy when waves are superimposed.

The complementary fields energy content of an electromagnetic wave with electric field amplitude $A(\mathbf{r}, t)$ and phase $\Phi(\mathbf{r}, t)$ is equal to

$$\mathcal{E} = \varepsilon A^2(\mathbf{r}, t)\frac{\partial\Phi(\mathbf{r}, t)}{\partial t}. \tag{2.30}$$

The energy density proposed in an earlier communication [12, eqs.(24)-(25)] has been scaled by the permittivity factor ε to establish the equality. This quantity represents the energy exchange between the two complementary fields. Whereas the flow is equal to

$$\mathbf{S}_{\perp} = \frac{1}{\mu} A^2 (\mathbf{r}, t) \nabla \Phi (\mathbf{r}, t) . \tag{2.31}$$

The exchange energy flow can be written in terms of the temporal derivative since $\nabla \Phi = \frac{\partial \Phi}{\partial t} \left(\frac{\hat{\mathbf{k}}}{v} \right) = \sqrt{\mu \varepsilon} \frac{\partial \Phi}{\partial t} \hat{\mathbf{k}}$, where $\hat{\mathbf{k}}$ is a unit vector in the direction of propagation. The flow of the exchange energy is then

$$\mathbf{S}_{\perp} = \sqrt{\frac{\varepsilon}{\mu}} A^2 (\mathbf{r}, t) \frac{\partial \Phi (\mathbf{r}, t)}{\partial t} \hat{\mathbf{k}}. \tag{2.32}$$

The impedance is often written in optics for non magnetic media as $\sqrt{\frac{\varepsilon}{\mu}} = \varepsilon \frac{c}{n} = \varepsilon_0 c\, n$. For a plane monochromatic wave (labeled with subindex j), the amplitude is constant $A_j (\mathbf{r}, t) = A_j$ and the phase is linear in the time and space variables $\Phi_j (\mathbf{r}, t) = \mathbf{k}_j \cdot \mathbf{r} - \omega_j t$, where the wave vector $\mathbf{k}_j$ and the angular frequency ω_j are constant. The assessed quantities (2.30) and (2.31) are then also constant

$$\mathcal{E} = \varepsilon A_j^2 \omega_j, \qquad \mathbf{S}_{\perp} = \varepsilon_0 c\, n A_j^2 \omega_j \hat{\mathbf{k}}_j. \tag{2.33}$$

Two issues should be highlighted, the frequency dependence of the energy density and the fact that no cycle averages have been performed. The linear frequency dependence means that when summing up over the phase locked monochromatic fields there is a frequency weighing factor. On the other hand, since no cycle averages are performed the energy density gives the instantaneous energy content of the wave-field.

2.5.1. Superposition of fields

The energy content of the sum of two or more fields is not equal to the sum of their individual energies but in the case of incoherent superposition. To wit, consider that the fields coexist in a certain region of space-time but there is no medium that allows for the superposition of the fields, that is, the fields do not sum up. The energy content of the jth monochromatic wave from (2.33) is

$$\left| \mathbf{S}_{\perp j} \right| = \varepsilon_0 c\, n\, A^2 (\omega_0 + j\delta\omega) ,$$

since the modes are equally spaced by $\omega_j = \omega_0 + j\delta\omega$ and $A_j = A$. If the waves are not added, the total energy is equal to the sum of energies of each monochromatic wave is

$$\sum_{j=m_i}^{m_f} \left| \mathbf{S}_{\perp j} \right| = \varepsilon_0 c\, n \sum_{j=m_i}^{m_f} A^2 (\omega + j\delta\omega) = \varepsilon_0 c\, n \left(m_f - m_i + 1 \right) A^2 \left(\omega + \left(\frac{m_f + m_i}{2} \right) \delta\omega \right) ,$$

that can be written as

$$I_{tot} = |\mathbf{S}_{\perp tot}| = \sum_{j=m_i}^{m_f} \left| \mathbf{S}_{\perp j} \right| = \varepsilon_0 c\, n\, m_{tot} A^2 \overline{\omega} \tag{2.34}$$

where $m_i = 1$, $m_f = m_{tot}$, the initial mode is one and the final mode equals the total number of modes m_{tot} and the mean mode angular frequency is $\overline{\omega} = \omega + \frac{m_{tot}+1}{2}\delta\omega$. The medium bandwidth gain is $\triangle\omega = (m_{tot} + 1)\,\delta\omega$. Notice that the total energy flow as well as the energy flow of each mode are time independent.

In the presence of a material medium, the Ti:Sa crystal in the laser oscillator case, the modes interact via the gain medium. The medium thus responds to the superposition of the fields. In this case, it is the energy of the superimposed fields that needs to be evaluated. The energy content of the coherent sum from (2.30) and (2.26) is

$$I_{coh} = |\mathbf{S}_{\perp coh}| = \varepsilon_0 c\, n\, A^2 \left[\frac{\sin\left(\frac{m_{tot}\delta\omega\, t}{2}\right)}{\sin\left(\frac{\delta\omega\, t}{2}\right)}\right]^2 \overline{\omega}.$$

The energy of the sum of waves is now time dependent and sharply peaked at $\delta\omega\, t = 2\pi b$ for integer b. The maximum intensity is

$$I_{max} = |\mathbf{S}_{\perp coh-max}| = \varepsilon_0 c\, n\, A^2 m_{tot}^2 \overline{\omega}. \tag{2.35}$$

However, this result does not necessarily imply that there has been an energy redistribution in time. It does mean that a device or entity capable of responding to the sum of the fields, such as an electric charge, will detect a large amplitude at the peaks. Outside this region, from the comparison of (2.34) and (2.35), it will detect an intensity approximately $1/m_{tot}$ lower.

3. Medium gain and mode locking operation

3.1. Gain without mode-locking.

The second curved C2 mirror was varied without mode locking while maintaining the slit width (S-W) totally opened (7.73 mm). The IR power output was recorded with a thermopile power detector [2]. The center wavelength was measured with two different monochromators. On the one hand, a scanning Czerny Turner monochromator, 0.5 m focal length[3]. On the other hand, a miniature fiber optic Czerny Turner spectrometer, 0.075 m focal length [4] with 2048 pixels detector array. The C2 mirror distance to the crystal is smaller for larger micrometer readings (see figure 1). The integration time in this latter system was 259 ms. The position was scanned from 9.60 mm up to 10.75 mm. From 9.60 mm to 10.30 mm it was varied in 0.10 mm steps. In the interval between 10.30 mm and 10.75 mm the variation was in steps of 0.05 mm.

Figure 7 shows the overlap of two runs. The output power lies around 200 mW between 9.9 and 10.7 mm C2 mirror position. The gain falls off rapidly before or after this range. However, there is a dip at 10.50 mm. This decrease is due to lasing operation at two CW wavelengths as shown in figure 8.

[2] Ophir 3A with Nova 2 meter, 3% accuracy
[3] Pacific MP-1018B
[4] Avantes AvaSpec 2048

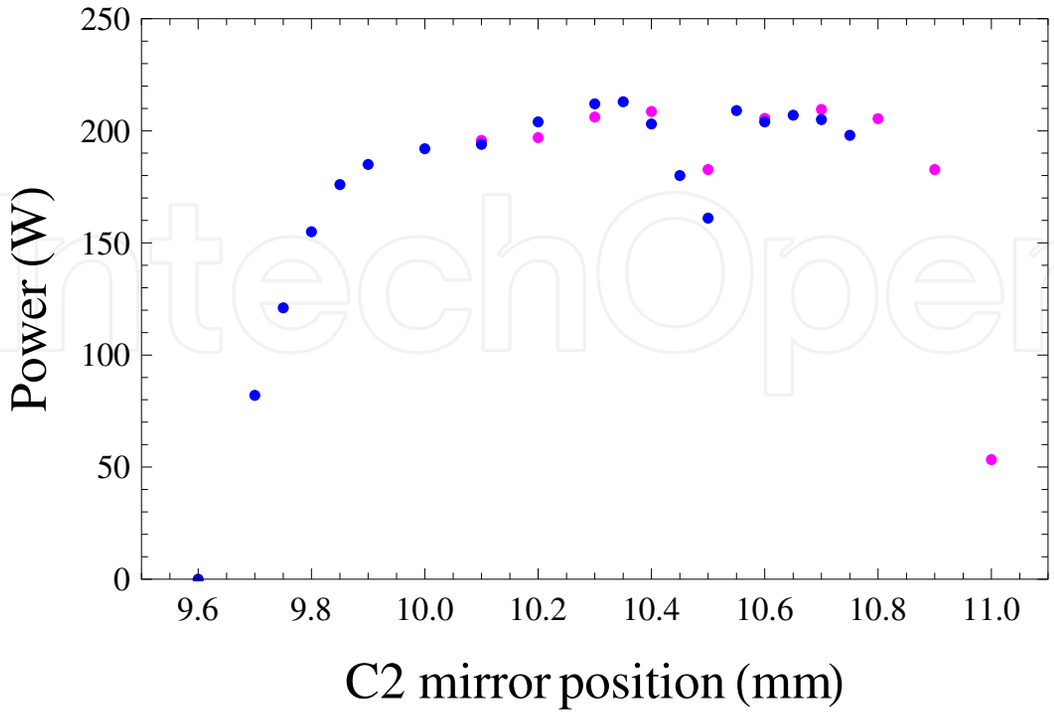

Figure 7. Mirror position vs. output power in non-mode locked operation. Points in pink were recorded directly on the computer whereas the blue ones were taken from the thermopile meter.

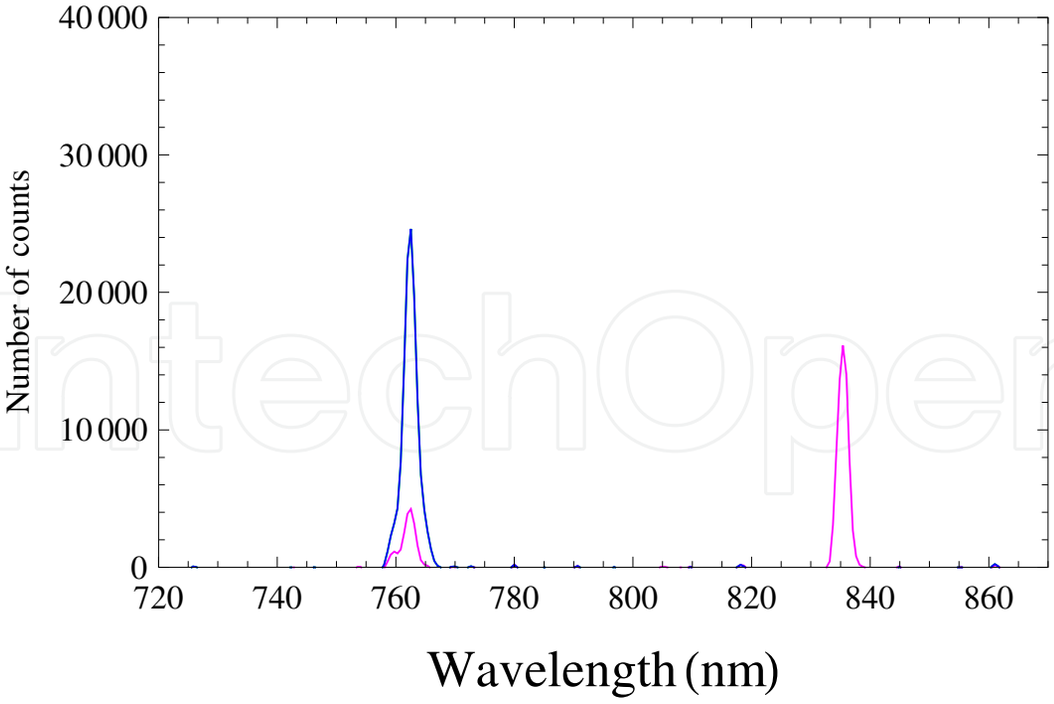

Figure 8. Continuous wave (CW) non-mode locked emission at 9.70 mm (blue) and 10.50 mm (magenta) depending on C2 position. Monochromator integration time is 259 ms.

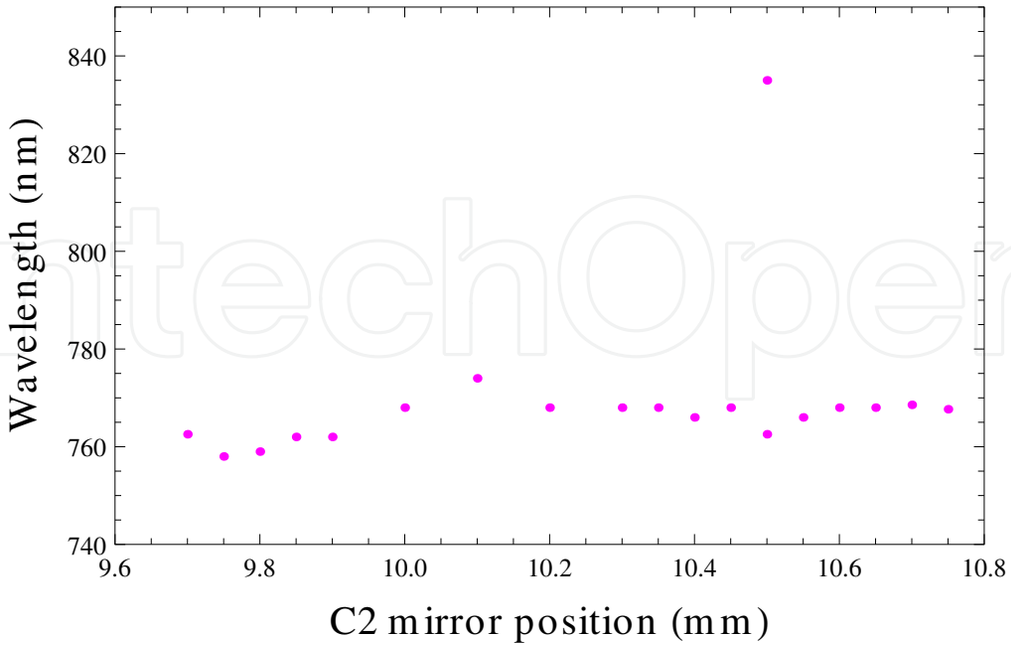

Figure 9. Emission wavelength vs C2 mirror position.

Figure 9 shows the wavelength where the maximum emission took place when C2 mirror was varied. The wavelength remains between 758 nm and 774 nm with the exception of the point at 10.50 mm, that emits at 762.6 nm and 835 nm.

3.2. C2 adjustment in mode-locking operation.

The focusing point within the active medium can be varied with the second curved mirror (C2) in order to obtain mode locking operation [14]. The position when self focussing of the intense beam attains maximum overlap with the pumped region will produce pulsed operation. This position lies on the edge of the gain curve (10.80 mm lies on the right hand border in figure 7). It is necessary to be within the gain curve so that many modes are amplified. However, if some modes experience a very large gain they will prevail over the pulsed many mode superposition. There are two ways to suppress this continuous (CW) light breakthrough: 1) lowering the pump current of the seed laser beam and 2) by moving the second curved mirror C2 [5]. To get the maximum power optimization the second option was chosen. Mode locking operation without CW breakthrough was obtained from 10.81 mm to 10.85 mm micrometer reading as shown in figure 10. Beyond the 10.85 position laser operation was not sustained. The spectrum profile shifts towards longer wavelengths as the beam is focused further into the crystal. From 10.80 mm to 10.81 mm the amplitude decreases due to less overlap between the focused beam and the gain region. Thereafter the amplitude remains constant presumably because self-focusing compensates and focuses the beam within the gain volume. On the other hand, the continuous light CW breakthough vanishes at 10.83 mm position. For C2 greater than 10.83 there is no CW breakthrough because no single mode is amplified above other modes.

[5] Quantronix, Ti-Light Operator's manual.

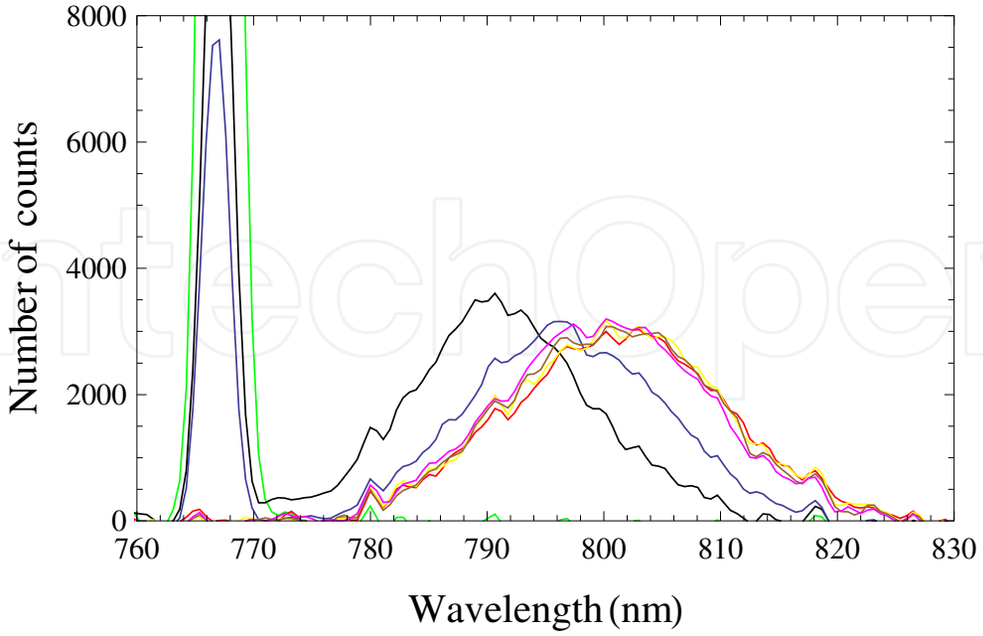

Figure 10. Spectra for different C2 mirror positions. At 10.80 mm two spectra were taken, with (black) and without (green) mode locking . All other spectra were made in mode locked operation; 10.81 mm (blue), 10.82 mm (red), 10.83 (yellow), 10.84 mm (brown) y 10.85 mm (magenta) (Curves from left to right). The continuous sharply peaked contribution vanishes when C2 mirror is located at 10.82 mm and further away. Spectrometer integration time is 259 ms.

4. Pulse train measurement and cavity length

4.1. Repetition rate

The output oscillator pulses were measured with an internal photo diode as well as a fast avalanche external photo diode. The internal photo diode is electronically amplified whereas the external photo diode was not amplified to provide the fastest possible risetime. Both signals gave similar results. The pulse repetition frequency was monitored with a fast oscilloscope[6]. The repetition frequency obtained from the scope trace shown in figure 11 is 77.5 ± 0.1 MHz with a period of $\tau = \frac{1}{\delta\nu} = 12.90 \pm 0.02$ ns which gives a round trip cavity of $\tau c = \frac{c}{\delta\nu} = 12.90 \times 10^{-9} \times 3 \times 10^8 = 3.86\,\text{m} = 2L$, thus the cavity optical length is $L = 1.928$ m. The angular frequency mode separation is then $\delta\omega = 2\pi\delta\nu = 486.9 \pm 0.6$ MHz or in wavelength units @ 800 nm, $\delta\lambda = -\delta\nu\frac{\lambda^2}{c} = -77.5 \times 10^6 \frac{\left(800\times10^{-9}\right)^2}{3\times10^8} = 1.65 \pm 0.02 \times 10^{-13}$m. For a typical bandwidth of 35 nm (see figure 22b) the number of modes is $m_{tot} = \frac{\triangle\omega}{\delta\omega} = \frac{35}{1.65\times10^{-4}} = 2.21 \times 10^5$. The coherent superposition of these modes gives a pulse width, according to (2.28)

$$\triangle t_{FW0} = \frac{1}{\delta\nu}\frac{2}{m_{tot}} = 12.9 \times 10^{-9}\frac{2}{2.21 \times 10^5} = 116\,\text{fs}.$$

[6] Tektronix 485/R485 analogue oscilloscope with 350 MHz bandwidth or Picoscope 5302 digital scope with 250 MHz bandwidth.

The measured pulse width is in this order of magnitude, although somewhat lower. Recall however, that this estimate is for the first zero rather than width at half maximum. Evaluation from FWHM series estimate (2.29) gives a closer estimate to the values reported in section (6),

$$\triangle t_{FWHM} = \frac{1}{2\pi\delta\nu}\frac{4\sqrt{3}}{m_{tot}} = 12.9 \times 10^{-9}\frac{1.1027}{2.21 \times 10^5} = 64.36\,\text{fs}.$$

Nonetheless, it should be stressed that pulse width is critically dependent on the pulse envelope. The spectra shown in subsequent sections were integrated over 259 ms as mentioned in section 3.1. Since the repetition rate is 77.5 MHz, the spectra show the average of 2.007×10^7 pulses.

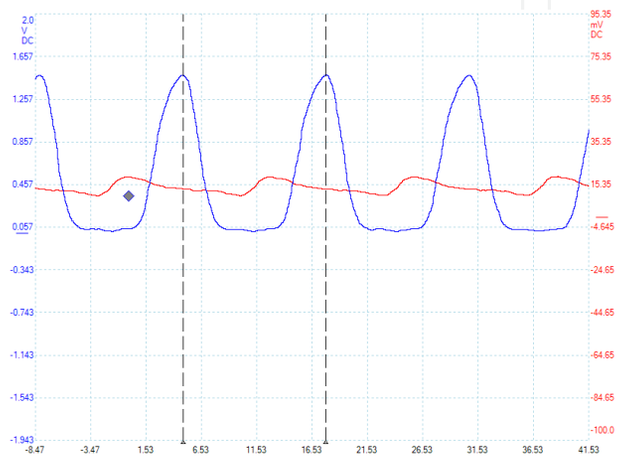

Figure 11. Oscillator output pulses detected with the internal photodiode (blue) and an external avalanche hamamatsu photodiode (red). The horizontal axis represents time in ns and the vertical axis depicts photodiode voltage.

4.2. Mode locking power and CW broadband background

An external fast photo diode was used to evaluate the difference between the mode locking (ML) peak intensity and the background light in between the high intensity peaks. This CW broad spectrum background light should not be confused with the CW narrow bandwidth breakthrough mentioned in subsection 3.2. The broad CW background is always present and is due to the superposition of the cavity modes when they are out of phase. Typical traces are shown in figure 12. The width of the peaks in the order of 1 ns are due to the detection system (photo diode + scope) since the optical pulse duration is four orders of magnitude shorter. The light level stabilizes at $I_{bb} = 10$ a.u. in between pulses. This measurement corresponds to the broad background (bb) emission between pulses in mode-locked operation. There is possibly electrical ringing after some pulses in the blue trace. In all three curves, there are spurious peaks due to analog to digital conversion uncertainty. This assertion is suported by the lack of subsidiary peaks in the streak camera recordings shown in the next section. The average intensity of the narrow bandwidth (nb) in non-mode locked operation is $I_{nb} = 6.3$ a.u. The ratio of these two intensities is $\frac{I_{bb}}{I_{nb}} = 1.59$. This quantity is an estimate of the energy content when a large number of out of phase modes (aprox. 10^5) are present in comparison with flow detected when a few modes are present.

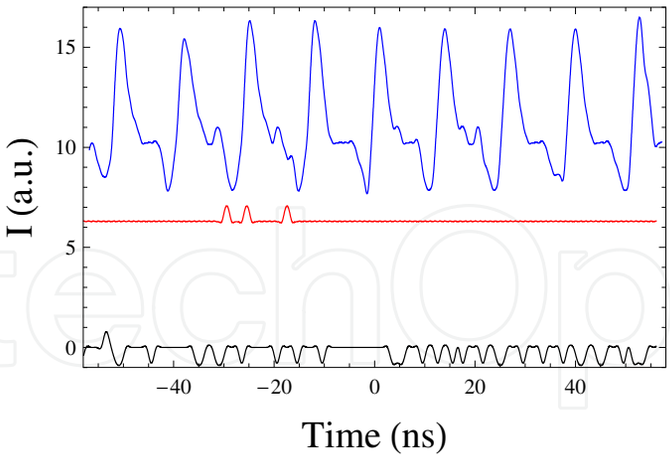

Figure 12. Oscillator pulse train detected with fast avalache photo diode and digital oscilloscope. Mode locked operation (blue trace), non-mode locked (red trace), residual trace with beam blocked in black. Small peaks are most likely due to analog to digital conversion uncertainty.

A streak camera was used to record the oscillator output. Firstly, a fraction of the laser beam output was fed through an optical fiber of 400 μ diameter and two fibers with 5 m length. This way the pulse was spread in time due to dispersion in the multimode fibre to insure that the peak intensity in the streak photocathode was not too high. The streak camera[7] was swept with a 330 ps/mm - 25 ns/mm sweep unit with 100 kHz maximum trigger frequency[8]. This unit was triggered by a pulse generator[9] that was in turn triggered by the laser oscillator electrical signal output. The unit was swept at 6.6, 10, 20, 50 and 100 ns full time bases. A typical intensity plot is shown in figure 13. The time span between pulses is $\tau = 13.12 \pm 0.5$ ns. The error is due to 2.5% non-linearity error in the time sweep. This result is consistent, within error, with the repetition rate obtained from the photo diode measurement.

5. Pulse spectrum and center wavelength

The pulse spectrum can be altered by the position of the second prism or the position and width of the slit placed between this prism and the end mirror.

5.1. Pulse spectrum as a function of prism compensation

In order to keep a narrow pulse, the two prisms are used to compensate the group velocity dispersion (GVD) introduced by the pulse propagation through the titanium sapphire crystal [15, 16]. The second prism (PR2) has a translational motion while the first prism position is fixed. The cavity design would benefit if the first prism (PR1) is also mounted on a traslation stage. The initial operating conditions are shown in table 2.

The spectrum in figure 14 shifts towards longer wavelengths as the second prism (PR2) position decreases. The wing on the right hand side of figure 14 shows that all the profiles

[7] Optronis SC-10
[8] Optronis TSU12-10PG sweep unit
[9] Stanford Research DGC535

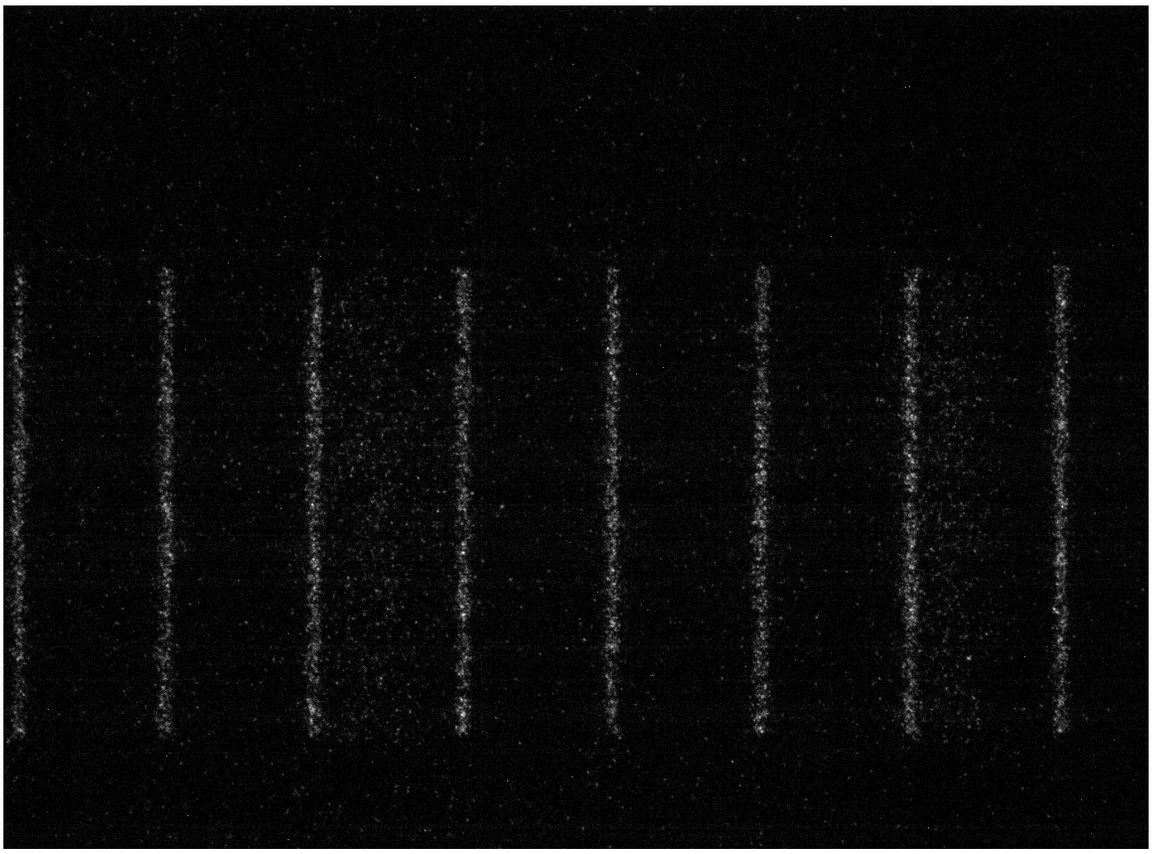

(a) Streak camera image. The vertical direction shows a transverse beam spatial direction and the horizontal direction represents the time axis.

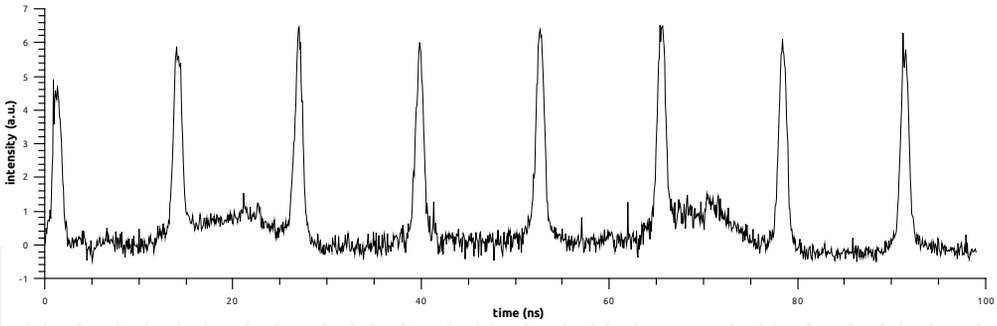

(b) Streak camera intensity time profile.

Figure 13. Streak camera image and graph of Ti:Sa oscillator pulses. The sweep rate is 5 ns/mm, 100 ns full sweep (small background bumps are due to pulses during backtrace).

converge towards 860 nm. However, the wings on the left hand side are displaced as the curve maximum is displaced towards shorter wavelengths. On the other hand, the amplitude increases at longer wavelengths and the bandwidth becomes narrower. In figure 15 a plot of the bandwidth as a function of the prism PR2 position is shown. Another set of spectra under the same operating parameters as shown in table 2 are depicted in figure 16. The same features described in the previous case are observed except for an amplitude decrease rather than increase at longer wavelengths. This discrepancy is possibly due to a slightly different cavity alignment so that shorter or longer wavelengths' gain were favoured in either case.

Element	Position (mm)
Mirror C1 position	3.98
Mirror C2 position	10.85
Lens L1 position	4.12
Prism PR2 initial position	1.30
Slit width (S-W)	7.73
Slit translation (S-T)	3.00

Table 2. Initial conditions when prism PR2 position was varied.

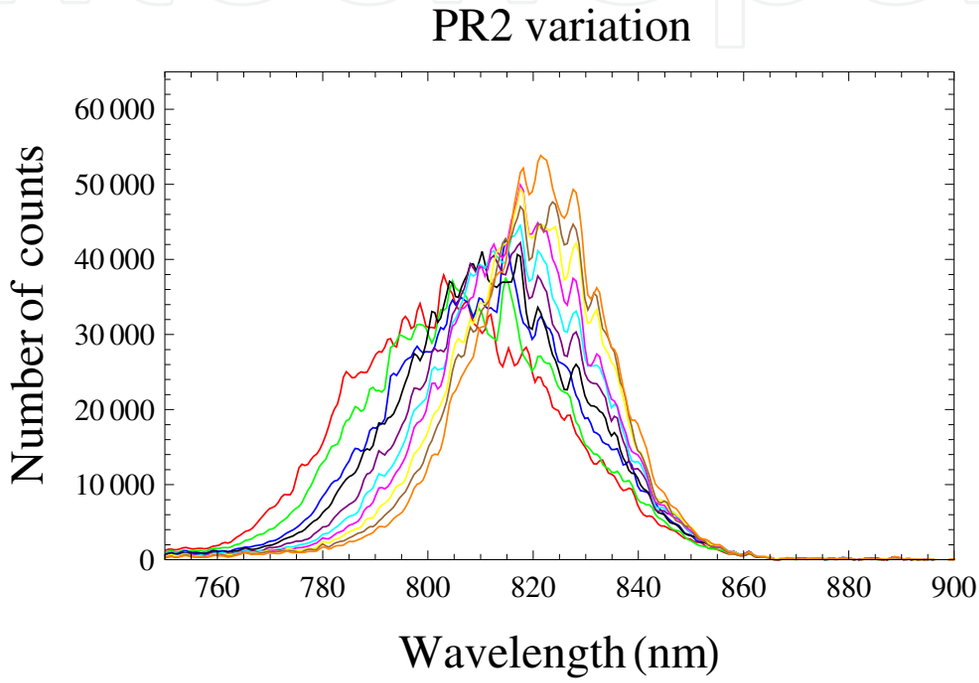

Figure 14. Spectra with mode lock taken at different prism PR2 positions: 0.40 mm(orange), 0.50 mm(brown), 0.60 mm(yellow), 0.70 mm(magenta), 0.80 mm(cyan), 0.90 mm(purple), 1.00 mm(black), 1.10 mm(blue), 1.20 mm(green) y 1.30 mm(red). The PR2 position was varyied by 0.10 mm steps. Spectrum curves shift towards longer wavelengths for larger micrometer readings.

The prism apex moves further into the beam as the micrometer reading increases (see figure 21a). As the beam travels through more prism material, the ML emission shifts towards shorter wavelengths.

5.2. Adjustment of the slit width (S-W)

The slit has two degrees of freedom, translation (S-T) and slit width (S-W) as can be seen in figure 17. Each of these displacements was varied separately.

The slit width micrometer is not calibrated to the real aperture width. The slit aperture was measured with a Vernier and a difference of 0.73 mm was obtained when the slit micrometer was set to zero. Hereafter, this value is added to slit width (S-W) micrometer readings in order to report the actual slit width. It should also be noted that one blade is fixed and only the blade

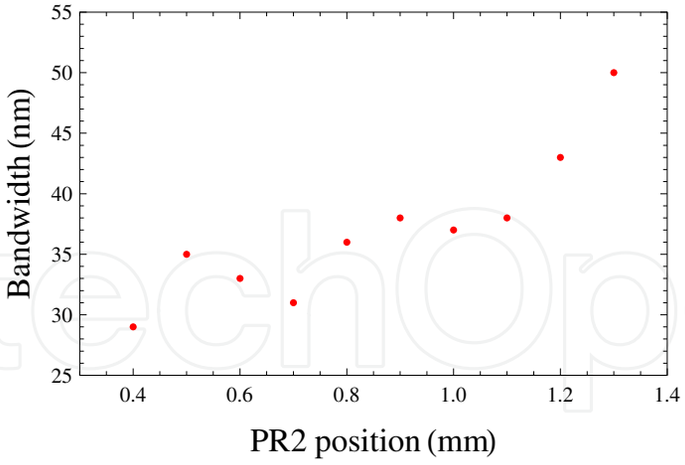

Figure 15. Bandwidth variation as a function of second prism (PR2) position. Micrometer readings between 0.40 and 1.30 mm.

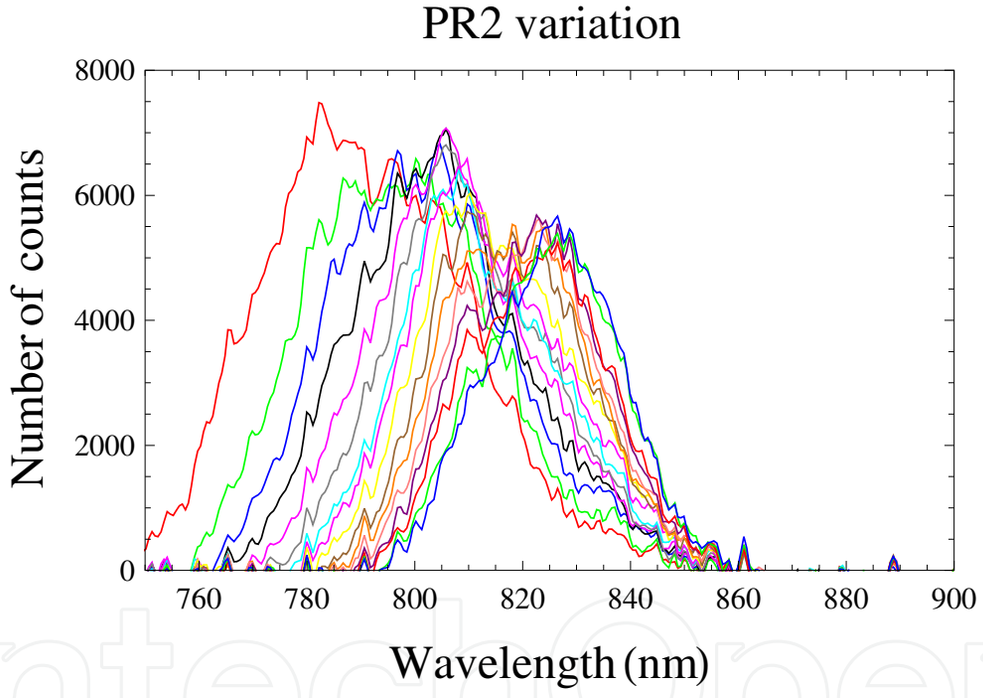

Figure 16. Spectra with mode lock for prism PR2 position between 0.00 and 1.50 mm: 0.00 mm (blue), 0.10 mm (green), 0.20 mm (red), 0.30 mm (purple), 0.40 mm (pink), 0.50 mm (orange), 0.60 mm (brown), 0.70 mm (yellow), 0.80 mm (magenta), 0.90 mm (cyan), 1.00 mm (gray), 1.10 mm (magenta), 1.20 mm (black), 1.30 mm (blue), 1.40 mm (green) and 1.50 mm (red). The position was varied in 0.10 mm steps. Micrometer readings decrease in curves from left to right.

on the blue side of the dispersion actually moves (see figures 21a and 17). The setup would benefit with a slit where both blades are displaced from a central position.

The laser parameters used while the width was changed are abridged in table 3. S-W was set at 3.73 mm and increased in steps of 0.50 mm up to 7.73 mm. Between 3.73mm to 7.73 mm the spectra did not show a noticeable variation because the laser beam is not blocked by the slit. That is, the beam width at the slit plane is smaller than the slit width. This assertion was

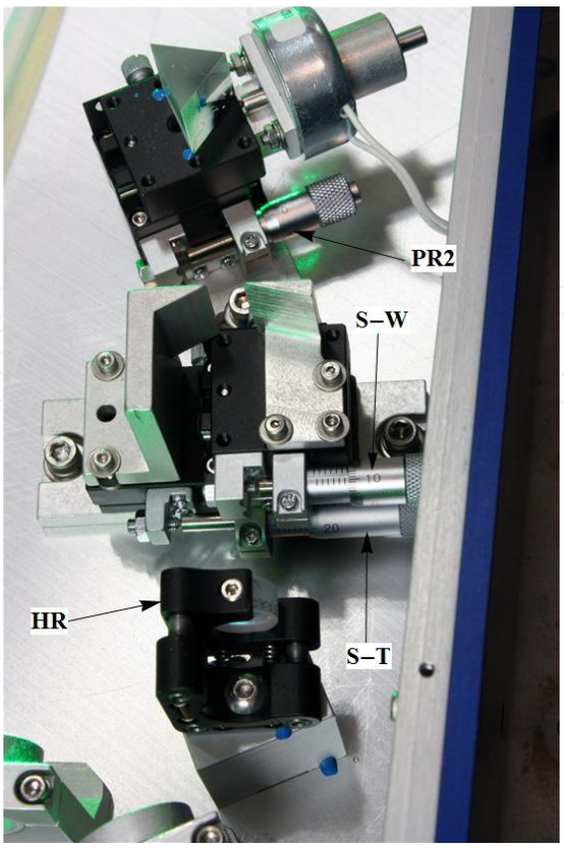

Figure 17. Slit displacement and width: S-T micrometer controls the translation mechanism whereas S-W alters the slit width.

confirmed by direct view with an IR viewer that no appreciable part of the beam was being blocked.

Element	Measurement (mm)
First curved mirror (C1)	3.98
Second curved miror (C2)	10.85
Pump beam focusing lens (L1)	4.12
Second prism position (PR2)	1.10
Initial S-W value	3.23
S-T position	5.50

Table 3. Initial conditions of slit width S-W variation .

The spectra for slit widths ranging from 3.23 to 1.43 mm are shown in figure 18. The S-W was decreased in 0.50 mm steps from 3.23 to 2.23 mm. Thereafter, it was decreased in steps of 0.10 from 1.93 to 1.43 mm. The spectra shifts towards longer wavelengths as the slit is reduced. This is expected because the moving blade crops from the blue side of the dispersion. On the other hand, the bandwidth decreases as the slit is closed although the intensity does not vary in an appreciable way. These features become relevant below the 2 mm width where the beam dispersion width is being considerably clipped. The pulse duration does not necessarily increase as the bandwidth is reduced until the pulse is time-bandwidth limited as we shall see in section 6.3.

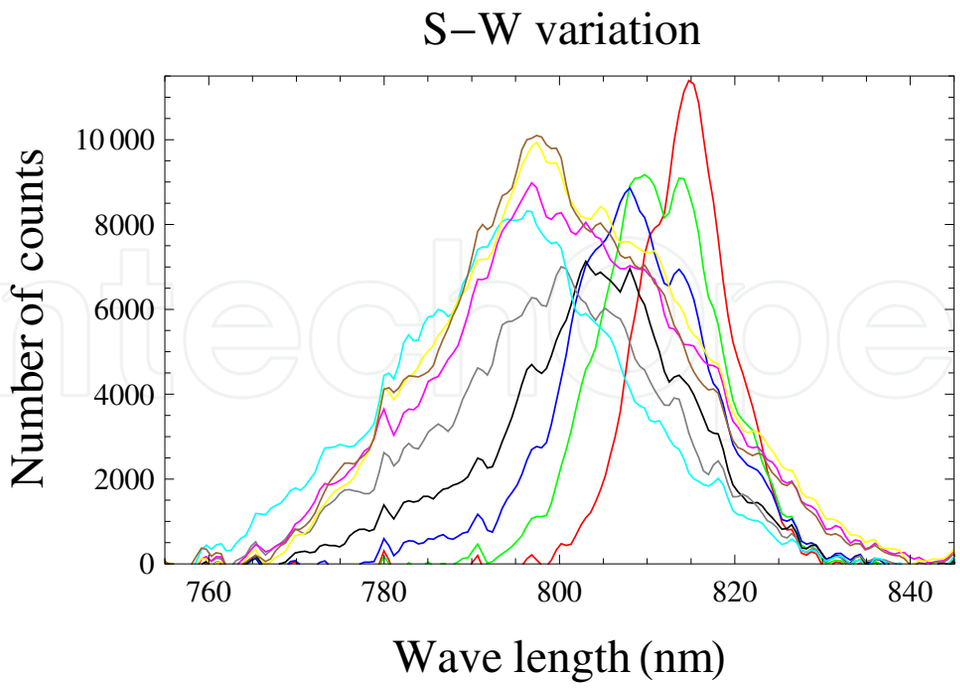

Figure 18. Spectra with mode lock for different slit widths: 1.43 mm (red), 1.53 mm (green), 1.63 mm (blue), 1.73 mm (black), 1.83 mm (gray), 1.93 mm (cyan), 2.23 mm (magenta), 2.73 (yellow) and 3.23 mm (brown). . From 2.23 mm to 3.23 mm the steps were of 0.50 mm. From 1.43 mm to 1.93 mm the S-W the steps were of 0.10 mm. Narrower slit width spectra lie on the right side of the figure.

5.3. Slit translation adjustment

The slit translation was varied from 7.60 mm to 0.40 mm while the slit width (S-W) was totally opened at 7.73 mm. The operating conditions while performing the S-T translation are shown in table 4.

Element.	Measure (mm)
First curved mirror (C1)	3.98
Second curved miror (C2)	10.85
Pump beam focusing lens (L1)	4.12
Second prism position (PR2)	0.5
S-W value	7.73
S-T initial position	7.60

Table 4. Initial conditions of S-T translation.

The spectra are shown in figure 19. ML emission is more intense at shorter wavelengths. The intensity decreases about tenfold for emission centered at 820 nm compared with emission centered at 730 nm. Nonetheless, stable operation is obtained from 730 to 850 nm, that is, in a 110 nm span. The curves suggest that emission can be obtained further to the blue but the micrometer mechanical translation table could not go any further.

In order to analyze these spectra we have separated the contributions in four different groups shown in figure 20. The slit translation (S-T) was decreased in steps of 0.10 mm from 7.60 mm to a 0.40 mm. At 7.60 mm the slit was blocking the redder frecuencies while the blue ones were

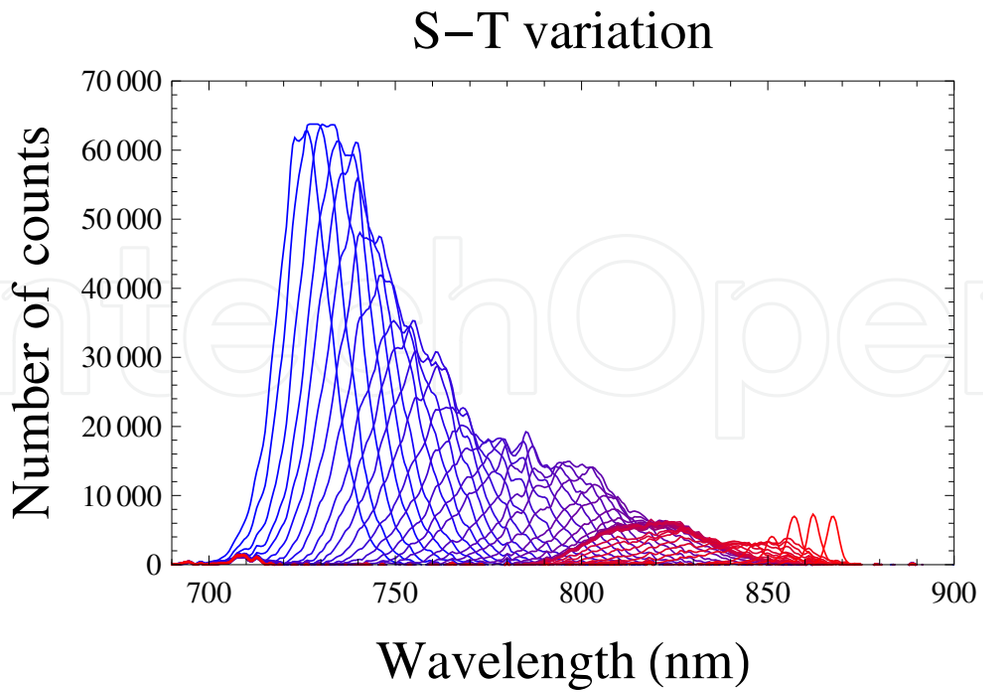

Figure 19. Mode locked spectra as a function of slit translation (S-T) from 7.60 mm to 0.40 mm. The spectrum varies from shorter to longer wavelengths and the intensity decreases for lower micrometer readings.

unblocked. A sketch of the slit together with the beam dispersed light is shown in figure 21a. Blue is dispersed at a larger angle than red in the first prism PR1 shown in photograph 21b. After a two mirror reflection it impringes on the second prism that is inverted with respect to the first one. When the slit was moved towards lower micrometer readings, the longer wavelength frequencies became progressively unveiled. As a result, the center wavelength moved towards longer wavelengths; The bandwidth increased and the spectrum intensity decreased as seen in figure 20a. At 5.20 mm the red side of the spectrum was completely unblocked.

From 5.10 mm to 3.50 mm, , the spectra do not suffer any change and the center wavelength remains constant as well as the bandwidth as shown in figure 20b. The beam is not blocked on neither side by the slit since the beam width is smaller than the slit width. This behaviour continued until the translation micrometer was at 1.60 mm.

Between 1.50 mm to 0.70 mm, the slit started to block the blue side of the spectrum while the red side remained unobstructed. The central emission thus shifts to longer wavelengths as seen in figure 20c. The bandwidth increases while the spectrum intensity continues to decrease.

Finally, from 0.80 mm to 0.40 mm the blue side of the spectrum is further blocked. However, the emission spectra in figure 20d show a different behavior. From left to right, the first two profiles exhibit a bandwidth reduction and an intensity increase on top of a much broader but lower intensity emission. The last three curves exhibit a central wavelength shift but the intensity remains constant while the broader emission is no longer present. This behaviour

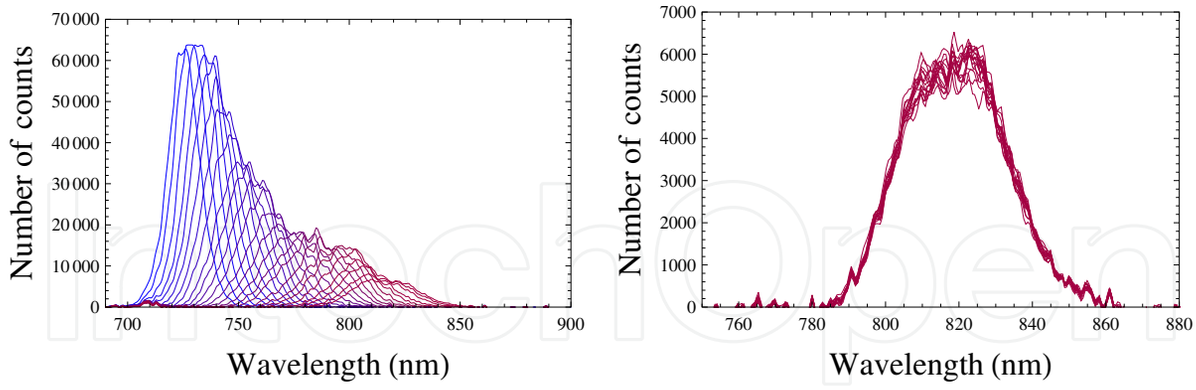

(a) S-T from left to right curves 7.60 mm to 5.20 mm in steps of 0.1 mm

(b) S-T between 5.10 mm to 3.50 mm

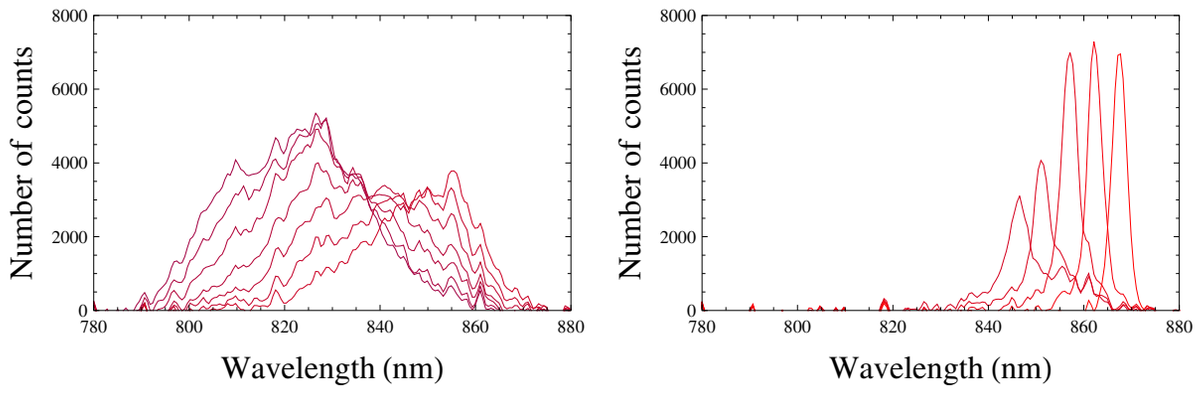

(c) From left to right S-T between 1.50 to 0.70 mm in 0.1 mm steps

(d) S-T between 0.80 mm to 0.40 mm

Figure 20. Oscillator pulse train spectra, with mode lock, as a function of slit translation (S-T). 20a) At higher micrometer readings the slit blocked most part of the beam frequencies on the red side. 20b) Does not exhibit any change in the spectrum since the beam is not blocked by the slit. 20c) For lower micrometer readings most part of the beam blue frequencies are blocked. 20d) Bandwiths are narrower when laser is hardly mode locking.

could suggest continuous light (CW) emission. However, even under these circumstances mode locking (ML) was still being held.

6. Pulse duration and time bandwidth product (TBP)

6.1. Frequency-Resolved Optical Gating (FROG)

FROG is a special kind of nonlinear autocorrelator that measures the pulse duration as well as other features of the pulse. This is possible because the autocorrelator signal beam is spectrally resolved. There are different kinds of FROG depending on the nonlinear medium: Polarization-Gate (PG), Self-Diffraction (SD), Transient-Grating (TG), Second-Harmonic-Generation (SHG) and Third-Harmonic-Generation (THG). Second-Harmonic-Generation is the most sensitive because it involves a second order nonlinearity rather than third. However, being an even order nonlinearity it is time

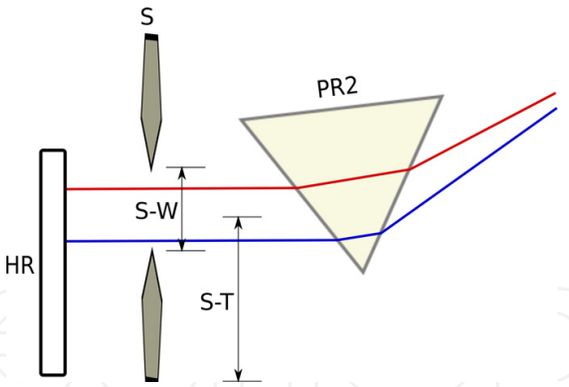

(a) Sketch of the intra-cavity mirror - slit - prism setup.

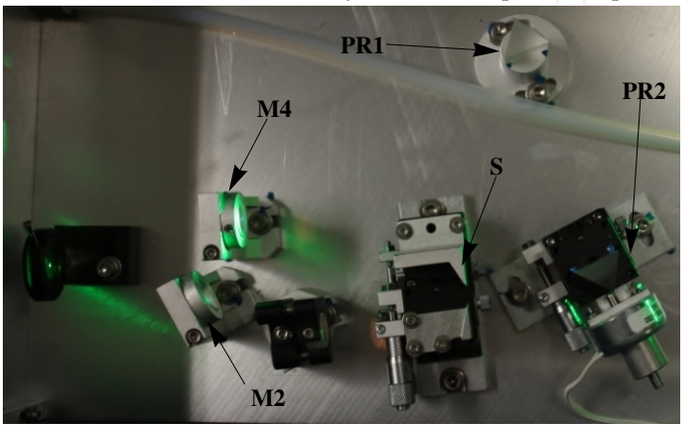

(b) Photograph of the mirror - slit and two prisms setup

Figure 21. Oscillator GVD compensating prisms and spectrum cropping slit. The solenoid that initiates mode locking operation can be seen below the second prism PR2.

symmetric and thus the time direction is ambiguous [17]. In the following experiments we used a simplifed FROG version called grenouille with a SHG crystal, 18 to 180 fs pulse duration measurement capability[10]. Grenouille raw data were processed with Femtosoft QuickFrog software. The pulse retrieval algorithm is reasonably reliable although it sometimes runs wild and it requires resetting. It gives numeric estimates of the pulse duration, TBP, central emission wavelength, pulse front tilt and spatial chirp. However, it does not state a temporal chirp value although the temporal phase curve is presented on screen.

6.2. GVD prism compensation and time bandwidth product (TBP)

The second prism (PR2) position was moved between 1.50 mm and -0.50 mm in steps of 0.10 mm. The initial parameters are summarized in table 5. From the data records, we produced plots of various pulse parameters in figure 22.

The pulse duration is plotted in figure 22a. It decreases as the prism PR2 micrometer reading is reduced. As we mentioned in section 5.1, the beam traverses less prism material as the micrometer reading decreases. The beam is incident on the apex of the first prism. In fact, a little bit of it on one side passes through without hitting the prism. It is expected that the

[10] GRENOUILLE 8-20 from Swamp optics

Element	Measurement(mm)
Mirror C1 position	3.98
Mirror C2 position	10.85
Lens L1 position	4.12
Prism PR2 initial position	1.50
Slit width (S-W)	7.23
Slit translation (S-T)	3.50

Table 5. Initial parameters when prism PR2 was moved.

second prism will produce a good GVD compensation when symetrically placed with respect to the first prism. The micrometer was moved until zero was reached and then moved further down as much as the mount allowed. In the innermost position the minimum time seemed to be reached. If the second prism over-compensates or under-compensates the first prism the pulse duration should increase. A minimum is expected when compensation is optimum. For this reason, we modeled the time duration curve with a quadratic fit

$$57.9953 + 12.8317(0.45 + x)^2. \tag{6.1}$$

The minimum time of the fit is located at 57.99 fs whereas the minimum experimental measurement was 62.4 fs. The bandwidth dependence is shown in figure 22b. It also decreases as the prism PR2 position is decreases. Again, a minimum is expected at optimum compensation. A quadratic fit is phenomenologically assigned

$$22.5591 + 2.79782(1.5 + x)^2. \tag{6.2}$$

While the time minimum seems to be reached at -0.5 mm, it is not clear that the bandwidth minimum has been reached yet. Indeed, the fit in equation (6.2) predicts that the minimum bandwidth is located at -1.5 mm.

The time-bandwidth product is plotted in figure 22c. This value was taken from the Frog retrieval algorithm. It should be proportional to the product of the previous two curves. A quadratic fit gives the following parameters

$$0.65104 + 0.381219(0.6 + x)^2. \tag{6.3}$$

The minimum TBP obtained from the fit is 0.65. However, the minimum TBP achieved with this setup is 0.783. This value is somewhat far from a fourier limited pulse as may be seen from comparison with table (6).

On the other hand the center wavelength increases as the prism position moves out of the beam as seen in figure 22d. A linear fit gives the equation

$$827.012 - 22.6234x. \tag{6.4}$$

This frequency dependence is similar to that observed in section (5.1).

The plot of the pulse front tilt is shown in figure 22e. When the two prism compensate each other transversely they should produce minimum pulse front tilt. However, according to

the frog measurements we are far from the minimum position. For this reason, although we expect a quadratic fit with a minimum, a linear fit was sufficient for the actual data

$$-11.8223 + 1.15039x. \tag{6.5}$$

It is not clear whether the pulse front tilt measurement is real or the Grenouille apparatus is slightly miscalibrated. A callibration experiment will be performed to elucidate this point.

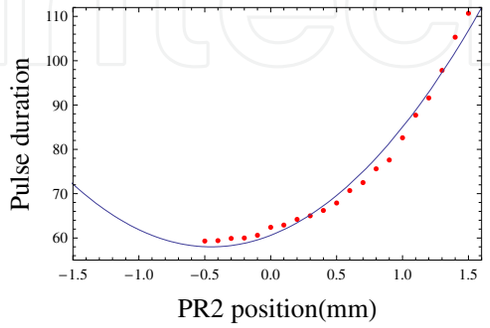

(a) Pulse duration $\triangle t$.

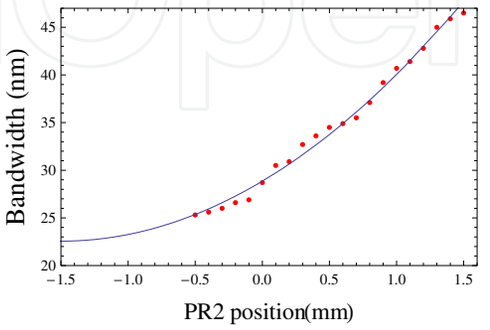

(b) Bandwidth $\triangle \lambda$.

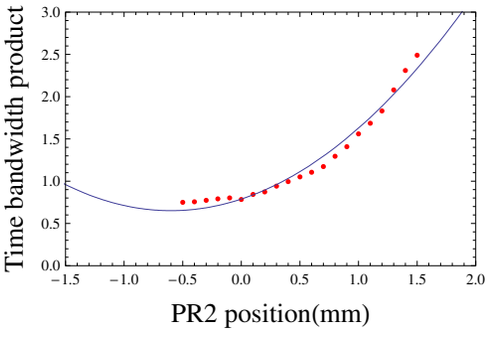

(c) Time bandwidth product (TBP).

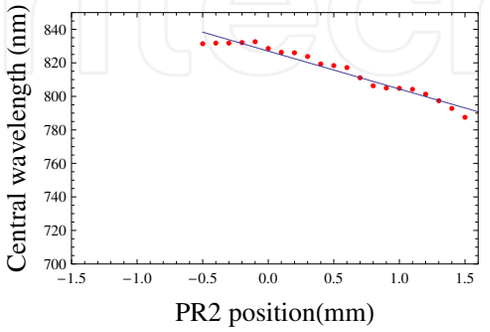

(d) Central emission wavelength λ_c.

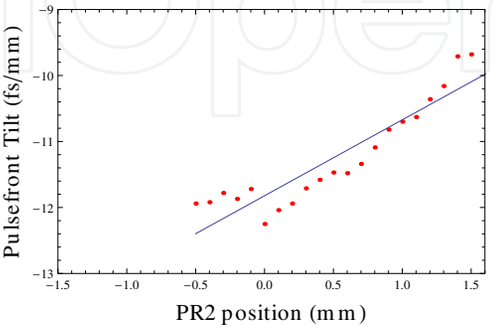

(e) Pulse front tilt (PFT).

Figure 22. $\triangle t$, $\triangle \lambda$, TBP, λ_c, and PFT versus prism PR2 position.

Since we did not achive a Fourier transform pulse, the bandwidth increases while the pulse duration increases too see figures 22a and 22b. Table 6 shows the different Fourier transform limits for different pulse shapes.

Envelope shape	$\varepsilon(t)$	Time bandwidth product
Gaussian function	$\exp\left[-(t/t_0)^2/2\right]$	0.441
Exponential function	$\exp\left[-(t/t_0)/2\right]$	0.140
Hyperbolic secant	$1/\cosh\left[t/t_0\right]$	0.315
Rectangle	-	0.892
Cardinal sine	$\sin^2\left[t/t_0\right]/(t/t_0)^2$	0.336
Lorentzian function	$\left[1+(t/t_0)^2\right]^{-1}$	0.142

Table 6. Fourier transform pulses for different shapes. Data taken from Rulliere et al. [14].

6.3. Spectrum cropping

The slit width (S-W) was varied between 1.43 mm and 7.23 mm. Table 7 shows the initial conditions for this experiment. It was varied in steps of 0.10 mm between 1.43 mm to 1.93 mm. From 1.93 mm to 2.73 mm the slit translation (S-T) was moved to center the laser beam within the aperture. Two different measurements at 2.73 mm on different days give an estimate of the measurement error in the various parameters shown in figure 23. Larger slit widths had little impact on the plotted parameters.

Element	Measurament(mm)
Mirror C1 position	3.98
Mirror C2 position	10.85
Lens L1 position	4.12
Prism PR2 position	1.50
Slit width initial width (S-W)	1.43
Slit translation (S-T)	3.50

Table 7. Initial conditions when S-W was varying

Let us now begin by describing the bandwidth behaviour that should be directly proportional to the slit width. Indeed, from 1.43 to 2.23 the experimental points lie on a straight line. At 2.23 mm the slit no longer crops the beam and thus becomes insensitive to slit width. The maximum bandwidth is around 35 nm consistent with the plateau shown in figure 15 in section 5.1.

The time bandwidth product dependence on slit width is shown in figure 23b. When the slit begins to crop the beam, the TBP decreases until it reaches the Fourier transform limit. A hyperbolic tangent fit of this curve is

$$0.816 + \frac{0.793}{2}\tanh\left[\frac{x}{0.259} - 4.677\right]. \tag{6.6}$$

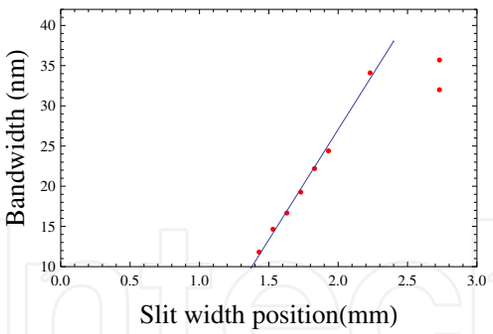

(a) Bandwidth $\triangle\lambda$.

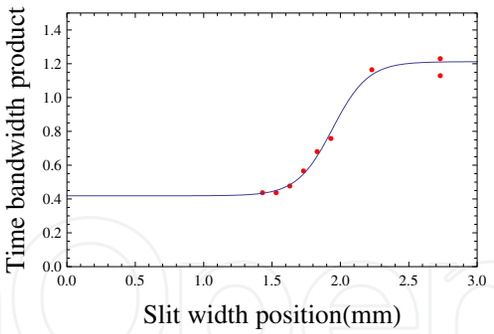

(b) Time bandwidth product TBP.

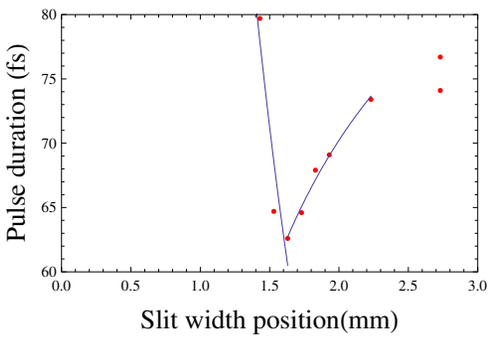

(c) Pulse duration $\triangle t$.

Figure 23. $\triangle\lambda$, TBP and $\triangle t$ versus slit width.

The minimum asymptotic value is $0.816 - \frac{0.793}{2} = 0.419$. This TBP is below the Gaussian envelope limit as seen from table 6, thus suggesting that the pulse envelope must be closer to the hyperbolic secant proposed for solid state lasers [8].

The time duration of the pulse versus slit width is shown in figure 23c. The experimental points show two rather different behaviors. On the one hand, the pulse duration decreases as the slit width is reduced between 2.73 and 1.63 mm. Beyond this value, the pulse duration increases as the slit width is further reduced.

This apparently wild behaviour of the pulse duration can now be nicely explained in terms of the bandwidth and the TBP. The pulse duration is reduced as frequency components far in the wings are cropped because these frequencies have a large spread in time due to dispersion. For large slit widths, the TBP follows the strict inequality product $\triangle t \triangle \nu > c_B$. Thus both quantities may decrease as long as the equality is not reached. However, when the TBP limit is reached, the pulse is Fourier transformed and it should fulfill the $\triangle t \triangle \nu = c_B$ equality. If $\triangle \nu$ (or equivalently $\triangle \lambda$) is further reduced as it happens beyond the 1.63 mm slit width, the time duration $\triangle t$ must increase so that the equality holds. The pulse duration in the Fourier transform limited region should fulfill an inverse relationship with slit width since

$$\triangle t = \frac{c_B}{\triangle \nu} \propto \frac{1}{\text{s-w}}.$$

The fit gives the following parameters

$$-0.818912 + \frac{55.2703}{x}\,. \tag{6.7}$$

For the non Fourier limited region the pulse width increases with increasing bandwidth. Since the bandwidth only increases up to the active medium - cavity maximum bandwidth it may also be fitted to an inverse function

$$89.8668 - \frac{24.7288}{x}. \tag{6.8}$$

The asymptotic value for this function is 89.86 fs.

A screen shot of the Fourier limited pulse (TBP=0.437) produced by the grenouille femtosoft software is shown in figure 24. The pulse duration is 64.7 fs and its bandwidth is 14.65 nm. The pulse exhibits a negligible temporal chirp as expected. Nonetheless and contrary to our expectations, the pulse front tilt is reported to be still rather large -10.3 fs/mm.

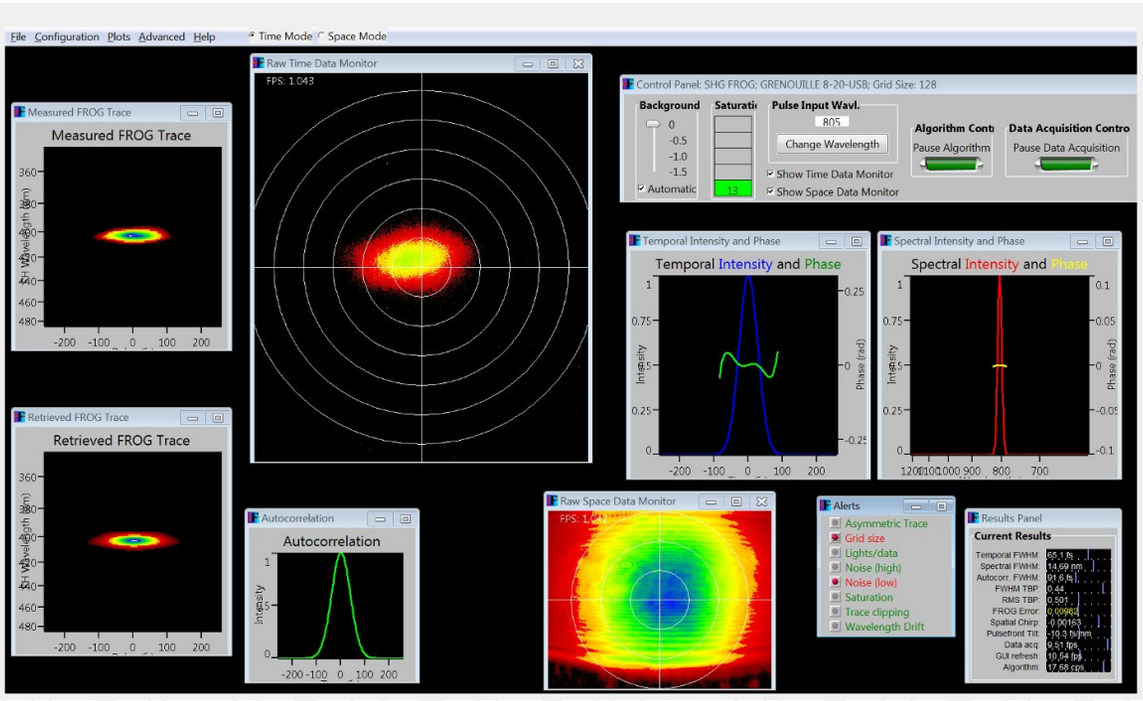

Figure 24. Screen shot for a Fourier limited pulse with slit width 1.53 mm. Grid characteristics 128 points; Delay increment: 4.03 fs; Center Wavelength: 807.3 nm Frog Error was: 0.01039 Temporal FWHM: 64.7 fs Spectral FWHM: 14.65 nm, FWHM Time-Bandwidth Product: 0.437, RMS Time-Bandwidth Product: 0.501.

6.4. Envelope shape

The data obtained from the frequency resolved optical gating measurements as well as the detailed spectra from integrated spectrometer measurements were analyzed in order to obtain the pulse envelope function. Two sets of spectra were analyzed. On the one hand, the spectrum optimized for minimum pulse duration and thereafter minimum TBP while maintaining the pulse duration. On the other hand, typical spectra shown in figure 20b, where the spectrum is rather broad and TBP is large.

6.4.1. Minimum pulse duration and minimum TBP spectrum

A Gaussian function without chirp (2.7) was fitted to the ML spectrum shown in figure 25. The parameters obtained without chirp are: $\tau_G \frac{2\pi c}{\lambda_l^2} 10^{-9} = 0.1086$, center wavelength $\lambda_\ell = 2\pi c/\omega_\ell = 809.628$ nm and the quality of the fit is $R^2 = 0.99770$. Once the time duration $\tau_G = 37.78$ fs was established from the previous fit, the Gaussian function with chirp (2.11) was fitted to the data. The fitted linear chirp parameter a was negligible $a = 4.02016 \times 10^{-8}$. The time duration obtained from the fit is $\triangle t_{FWHM} = \tau_G \cdot 1.17741 = 44.48$ fs. This fourier transform limited calculation underestimates the pulse duration given by the FROG retrieval measurement of 56.4 fs. If the TBP obtained from the FROG measurements is used in order to evaluate the Gaussian enevelope, $\tau_G = 53.43$ fs and the pulse width is $\triangle t_{FWHM} = 62.90$ fs; This time overestimates the FROG value by 11.5 %.

The hyperbolic secant function fit to the same data gave the following parameters: $\tau_s \frac{2\pi c}{\lambda_l^2} 10^{-9} = 0.06678$, center wavelength $\lambda_\ell = 2\pi c/\omega_\ell = 809.572$ nm and the quality of the fit is $R^2 = 0.99705$. Once the time duration τ_S was established from the previous fit, the hyperbolic secant function with chirp was adjusted. The chirp parameter was $a = 0.105855$. This small chirp parameter value improved slightly the curve fit, yielding $R^2 = 0.99790$.

The best fits with the Gaussian and hyperbolic secant envelopes give similar R^2 results. It is therefore not possible to discern whether the envelope follows one or the other profile under these conditions.

6.4.2. Typical spectra with broad spectrum and large TBP

A typical ML spectrum as shown in figure 20b was fitted to a Gaussian envelope function. Since the functional dependence of the pulse width τ_G and the linear chirp parameter a in the exponential argument are similar, no substantial difference is obtained when chirp is added. The Gaussian fit parameters are: $\tau_G \frac{2\pi c}{\lambda_l^2} 10^{-9} = 0.07079$, center wavelength $\lambda_\ell = 2\pi c/\omega_\ell = 817.608$ nm and the quality of the fit is $R^2 = 0.99105$ is rather poor.

The ML spectrum shown in figure 20b was fitted to a hyperbolic secant envelope function with and without chirp. The data are plotted against wavelength rather than frequency; Therefore the scaling $\Omega - \omega_\ell \rightarrow \frac{2\pi c}{\lambda^2}(\lambda - \lambda_c)$ is required. The frequency dependent sech^2 intensity function without chirp given by (2.21) has parameters $\tau_s \frac{2\pi c}{\lambda^2} = 0.0357$, centered at $\lambda_\ell = 2\pi c/\omega_\ell = 817.59$ nm and $R^2 = 0.98442$. On the other hand, the normalized intensity function with chirp function (2.24) was fitted with parameters: $\tau_s \frac{2\pi c}{\lambda^2} = 0.0649$, chirp coefficient $a = 1.122$ centered at $\lambda_\ell = 2\pi c/\omega_\ell = 817.56$ nm and $R^2 = 0.99472$. These fits are shown in figure 27. The function with temporal chirp is better adjusted due to the flat top of the central portion of the spectrum. The comparison between these fits is better visualized in a plot of the residuals shown in figure 28.

The hyperbolic secant function with chirp gives the smaller residuals and is thus the best fit. We can conclude that for oscillator pulses with considerable chirp, the pulse envelope is closer to a hyperbolic secant function.

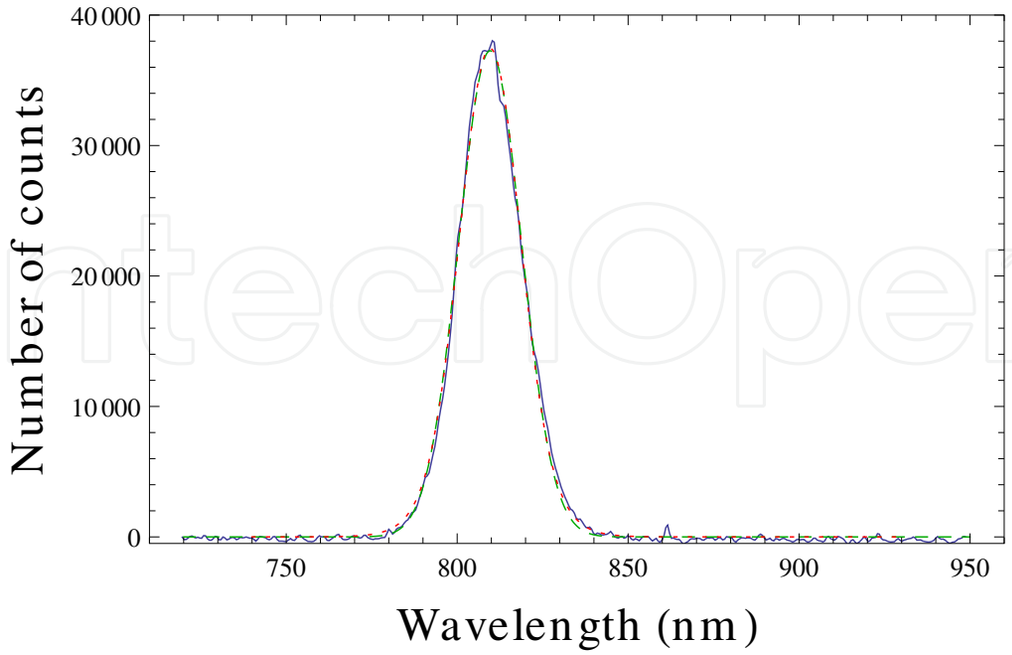

Figure 25. Spectrum of ML femtosecond oscillator taken with miniature spectrometer, 400 ms integration time. The oscillator parameters are optimized for minimum pulse duration (56.4 fs) and minimum TBP (0.624). Fits with Gaussian (dashed green line) and a hyperbolic secant (dotted red line) functions are shown. Fits with or without chirp make little difference.

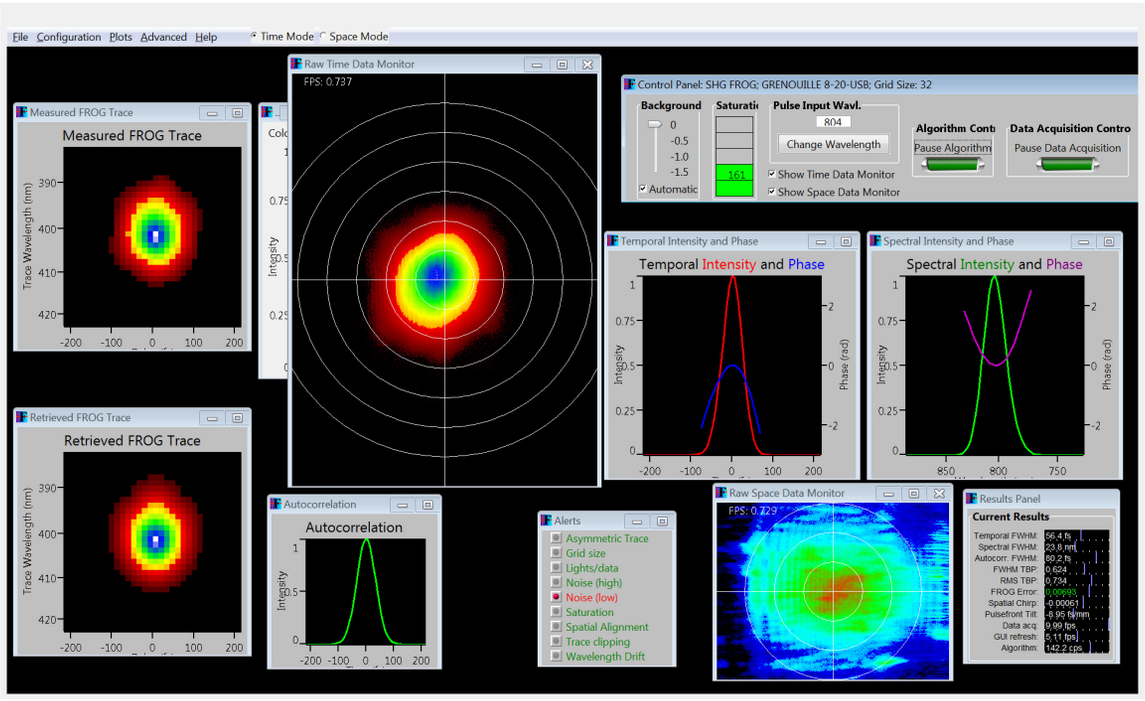

Figure 26. Screen shot for pulse with slit width 1.50 mm and slit translation 5.92mm. Center Wavelength: 809.6 nm Frog Error was: 0.00693 Temporal FWHM: 56.4 fs Spectral FWHM: 23.8 nm, FWHM Time-Bandwidth Product: 0.624.

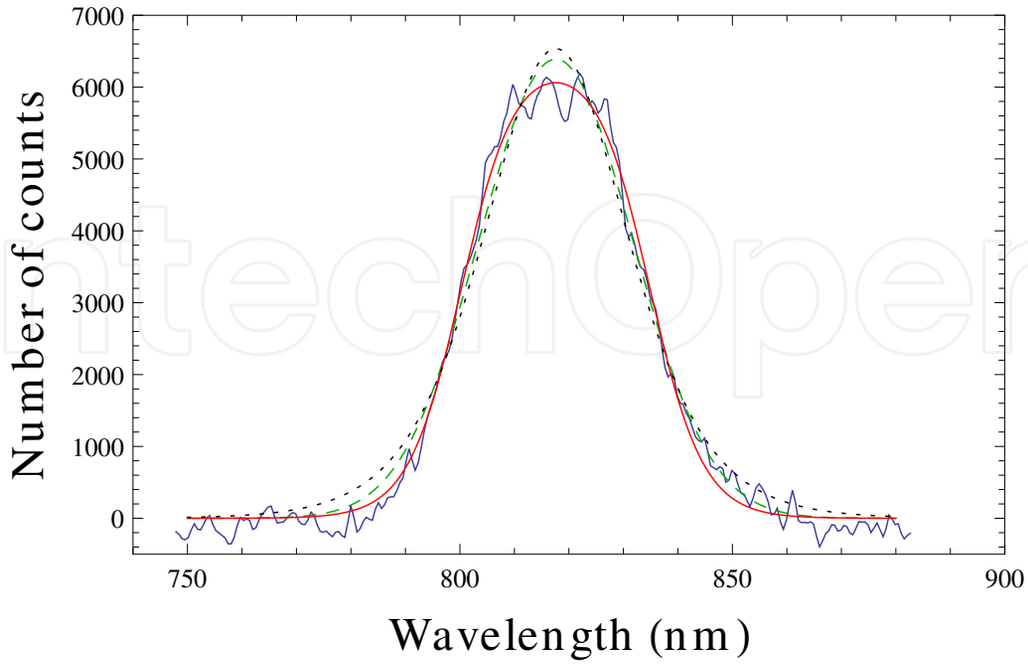

Figure 27. Gaussian (green dotted line) and Hyperbolic secant (HS) envelope fits to a typical spectrum (blue solid line) shown in figure 20b. The black dashed curve is a HS fit without chirp whereas the red continuous curve has a chirp factor of $a = 1.122$.

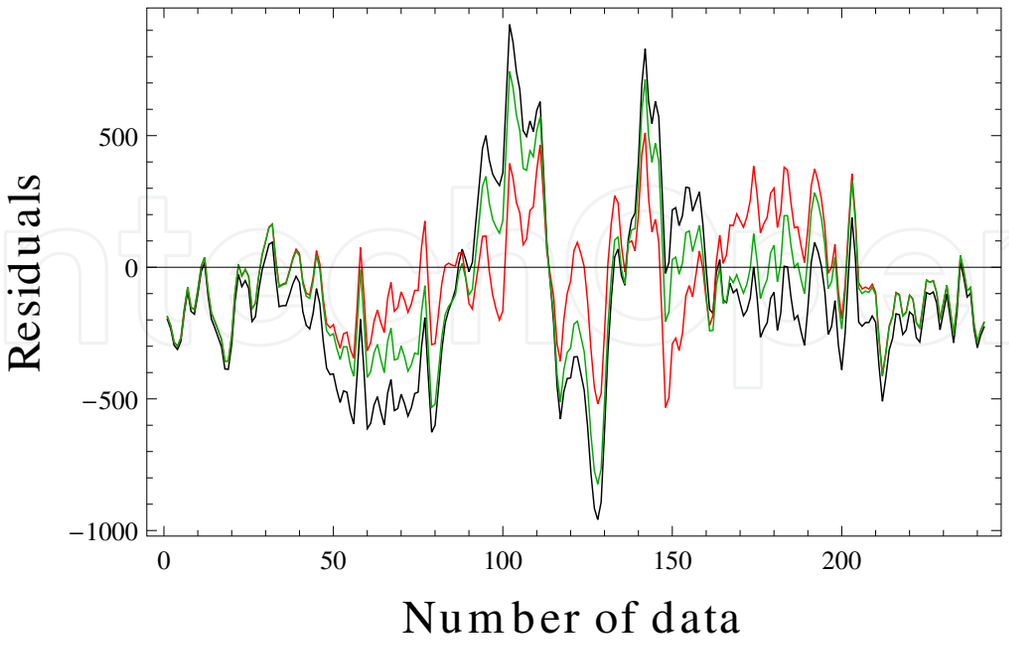

Figure 28. Residuals for the fits shown in figure 27. The Gaussian (green), Hyperbolic secant (HS) with (red) and without (black) chirp show that the best fit corresponds to the HS with chirp.

7. Conclusions

A Ti:Sa femtosecond laser oscillator was optimized for different operation purposes:

- A minimum pulse duration of 56.4 fs was obtained. The prims PR2 and the slit were adjusted to produce the minimum TBP of 0.624 while maintaining the shortest pulse duration.
- A time-bandwidth product of 0.783 with 62.4 fs pulse duration, 28.7 nm bandwidth and central wavelength of 828.6 nm was obtained when the prism PR2 was adjusted and the spectrum was not cropped.
- A Fourier limited pulse with time-bandwidth product of 0.437 with pulse duration between 63 to 79.7 fs, 11.82 to 18 nm bandwidth and central wavelength around 804.1 nm was obtained with appropriate bandwidth cropping with the intra-cavity slit.
- Oscillator emission was tuned from 730 to 850 nm with output power above 200 mW.
- The cavity adjustments would be more flexible if the first prism (PR1) is also mounted on a translation stage. A slit with two movable blades would also be welcome.

The wave description for Gaussian and hyperbolic secant envelopes was presented in detail. Results scattered in the literature were brought together in particular for the hyperbolic profile. The energy content of the wave field has been outlined with a novel continuity equation described in terms of complementary fields. These linearly independent fields do not require a temporal averaging over the pulse cycle. Therefore, they are well suited to describe ultrafast pulses or even few or single cycle pulses.

Acknowledgements

We are grateful to Raúl Rangel CISESE and his collaborators Jacob Licea Rodríguez and Alexandro Ruiz de la Cruz for useful comments and much needed advice.

Author details

E. Nava-Palomares, F. Acosta-Barbosa, S. Camacho-López and M. Fernández-Guasti.
Lab. de Óptica Cuántica, Depto. de Física, Universidad A. Metropolitana - Iztapalapa, 09340 México D.F., Ap. postal. 55-534, Mexico, url: http://luz.izt.uam.mx

8. References

[1] G. Muñoz, C. García, M. Muñoz, and M. Fernández-Guasti. Mesa holográfica pasiva ultra-estable: análisis de vibraciones. In *XXIII reunión anual de óptica*, sept 2010.

[2] Qiang Lin, Jian Zheng, Jianming Dai, I-Chen Ho, and X.-C. Zhang. Intrinsic chirp of single-cycle pulses. *Phys. Rev. A*, 81(4):043821, Apr 2010.

[3] Qiang Lin, Jian Zheng, and Wilhelm Becker. Subcycle Pulsed Focused Vector Beams. *Phys. Rev. Lett.*, 97(25):253902, 2006.

[4] J. C. Diels and W. Rudolph. *Ultrashort Laser Pulse Phenomena: Fundamentals, Techniques, and Applications on a Femtosecond Time Scale, Academic Press, 2nd edition, Elsevier 2006*. Elsevier Science Publishers, 2nd edition edition, 2006.

[5] M. Fernández-Guasti. The Wronskian and the Ermakov - Lewis invariant. *International Mathematical Forum*, 4(16):795 – 804, 2009.

[6] C. H. Henry. Theory of the linewidth of semiconductor lasers. *IEEE J. Quant. Elec.*, 18(2):259–264, 1982.

[7] T. L. Koch and J. E. Bowers. Nature of wavelength chirping in directly modulated semiconductor lasers. *Electr. Lett.*, 20(25/26):1038–1040, Dec 1984.

[8] P. Lazaridis, G.Debarge, and P. Gallion. Time-bandwidth product of a chirped sech2 pulses. *Optics Lett.*, 20(10):1160–1163, 1995.

[9] M. Fernández-Guasti, E. Nava, F. Acosta, and R. Chandrasekar. Physical processes behind a Ti:Sa femtosecond oscillator. In *Optics and Photonics 2011*, volume 8121 of *The nature of light: What are photons? IV*, pages 812118–1–10. SPIE, 2011.

[10] R. P. Feynman, M. Sands, and R. Leighton. *Lectures on physics*, volume II. Addison Weseley, 1972.

[11] M. A. Alonso. Wigner functions in optics: describing beams as ray bundles and pulses as particle ensembles . *Adv. Opt.Phot.*, 3:272–365, 2011.

[12] M. Fernández-Guasti. Complementary fields conservation equation derived from the scalar wave equation. *J. Phys. A: Math. Gen.*, 37:4107–4121, 2004.

[13] M. Fernández-Guasti. The necessity of two fields in wave phenomena. In *Optics and Photonics 2011*, volume 8121 of *The nature of light: What are photons? IV*, pages 81210R–1–12. SPIE, 2011.

[14] Claude Rulliere, editor. *Femtosecond laser pulses*. Advanced texts in physics. Springer, 2nd edition, 2005.

[15] O. E. Martinez, J. P. Gordon, and R. L. Fork. Negative group-velocity dispersion using refraction. *J. Opt. Soc. Am. B*, 1(10):1003–1006, October 1984.

[16] O. E. Martinez. Grating and prism compresors in the case of a finite beam size. *J. Opt. Soc. Am. B*, 3(7):929–934, July 1986.

[17] R. Trebino. *Frequency resolved optical gating*. Kluwer Academic Publ., 2000.